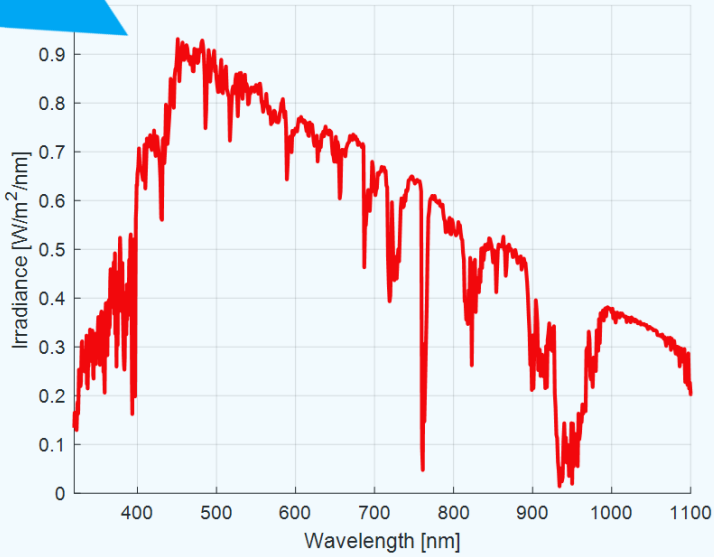
Spectral irradiance reconstruction model

In MATLAB utilizing a spectrally resolved albedometer

Wijnand Meines





TU Delft

Spectral irradiance reconstruction model

In MATLAB utilizing a spectrally resolved albedometer

by

Wijnand Meines

in partial fulfillment to obtain the degree of Master of Science
at the Delft University of Technology,
to be defended publicly on Friday October 7, 2022 at 9:00 AM.

Student number:	4444973	
Project duration:	Feb 7, 2022 – Oct 7, 2022	
Thesis committee:	Prof. I. Gordon,	TU Delft
	Dr. M. Cvetkovic,	TU Delft
	Dr. H. Ziar,	TU Delft, supervisor
	Ir. A. Martinez Lopez,	TU Delft, (daily) supervisor

This thesis is confidential and cannot be made public until October 7, 2024.

An electronic version of this thesis is available at http://repository.tudelft.nl/.

TU Delft

Preface

This report is written as part of the Master Thesis project from the Sustainable Energy Technology Master at Delft University of Technology.
I would like to thank everyone that helped and supported me in the last 8 months, but especially Arturo. Thank you for the weekly minutes with the nice discussions, and especially for taking the time during the last few weeks when you was also very busy to give feedback on my report.

Wijnand Meines
Delft, Oct 2022

Abstract

Bifacial modules are expected to have a 60% share in the PV market, which require spectral irradiance data incident on both sides to optimize the design. Sensors that provide spectrally resolved data are expensive and thus a cost-effective spectrally resolved albedometer was designed in two previous PVMD Master Theses. This albedometer measures irradiance in three wavelength bands. The focus of this research is on developing a model that reconstructs the spectral irradiance incident on the top part of the albedometer.

The spectral simulation program SMARTS was converted to MATLAB, after which a Particle Swarm Opimization Algorithm was added to determine values for unknown parameters. The model was first tested against spectra generated by SMARTS. After which both the original model and an model with additional modification coefficients was tested with clear-sky measurements from the albedometer and validated against an EKO spectroradiometer.

The original model proved to fail in the first wavelength band, which caused the other wavelength bands to be reconstructed poorly as well. The adjusted model performed close to the performance of the EKO for clear-sky irradiances above 400 W/m^2 in the total albedometer region, 320-1100 nm.

Contents

1 Introduction **1**

2 Background **3**
2.1 Solar irradiance . . . 3
2.2 Albedo . . . 5
2.3 Existing measurement technology . . . 5
2.3.1 Non-spectral measurement devices . . . 5
2.3.2 Spectral measurement devices . . . 7
2.4 Spectral simulation models . . . 8
2.5 Previous research at the PVMD . . . 8

3 Methodology **11**
3.1 SMARTS . . . 11
3.1.1 Direct Normal Irradiance . . . 11
3.1.2 Diffuse Horizontal Irradiance . . . 16
3.2 Spectrafy™ method . . . 16
3.3 PVMD albedometer approach . . . 17

4 Design of reconstruction model **19**
4.1 Particle swarm optimization . . . 19
4.1.1 Input parameters . . . 20
4.1.2 Optimization parameters . . . 21
4.1.3 Error function . . . 21
4.2 Assumptions and Limitations . . . 22
4.3 Reconstruction with respect to SMARTS spectra . . . 23

5 Measurement data and albedometer calibration **25**
5.1 Dataset . . . 25
5.2 Linear calibration . . . 27
5.2.1 Clear Sky data calibration . . . 29
5.3 Elevation angle adjustment . . . 31
5.4 Remarks . . . 34

6 Reconstruction results & analysis **35**
6.1 Reconstruction results . . . 35
6.2 Modified reconstruction results . . . 40

7 Conclusions and recommendations **45**
7.1 Conclusions . . . 45
7.2 Recommendations . . . 46

1

Introduction

Solar PV is the fastest growing renewable energy technology, accounting for 50-60% of the renewable added capacity from 2017 to 2023. (IEA, 2022). Within the Solar PV a shift is started from monofacial modules to bifacial modules, which are expected to account for over 60% of the total solar PV installed in 2032 Figure 1.1. Bifacial modules convert solar irradiance incident from both sides of the module. Next to irradiance incident on the front side of the panel, irradiance that is reflected by the surface below the module towards the module is also converted into energy. While this increases the efficiency of the PV modules, it also introduces a problem. Accurate energy yield predictions now require information about this reflected irradiance. The ratio between the reflected irradiance from a surface and the irradiance incident on the surface is called the albedo (Ziar et al., 2019). The albedo is usually described as a single value, which indicates the fraction of the total intensity of light that is reflected by a surface. For solar PV, and especially bifacial modules it is however also important to know the wavelength dependent, or spectral albedo. The spectral albedo is denpendent on material properties, but also on the spectral irradiance. A white obtject reflects almost all light incident on it, which makes it appear white under normal sunlight. If the sun is replaced by a red light, the object now appears to be red.

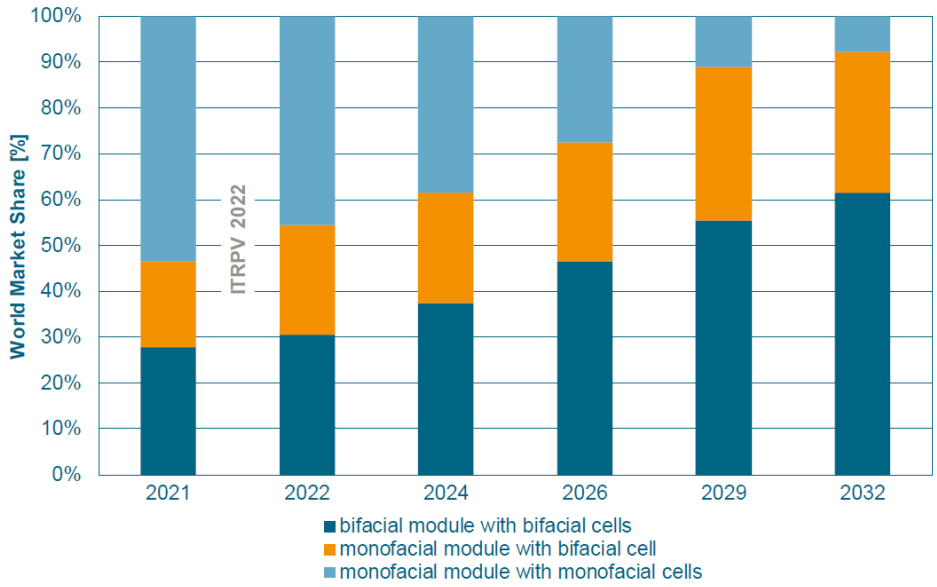


Figure 1.1: Predicted market share of monofacial and bifacial modules from 2021 to 2032 (VDMA, 2022)

In two previous Master Theses projects, an albedometer that measures the spectrum in three wavelength bands was developed and installed at the PVMD monitoring station (Romero Olvera, 2021) (Kaul, 2020). The Master thesis project presented in this report continues the work on this albedometer, focusing on obtaining spectra incident on the top part of the sensor. Besides the use of these spectra for obtaining the spectral albedo when the spectra incident on the bottom part can also be reconstructed, the spectra incident on the top part of the sensor can also be used to improve energy yield predictions and design for all PV modules.

The objective of this Master thesis project is to design a reconstruction model that simulates clear-sky solar spectra with limited irradiance inputs from a spectrally resolved albedometer designed in previous Master thesis projects by (Romero Olvera, 2021) and (Kaul, 2020) and installed at the PVMD montioring station. The reconstruction approach is based on the SMARTS program (Gueymard, 2001) and the method of Spectrafy, a company that has succesfully combined irradiance measurements with spectral simulation software to reconstruct solar spectra (Tatsiankou et al., 2014). The questions to be answered is with what accuracy the model can predict clear-sky solar spectra compared to an EKO™ spectroradiometer, which input parameters are required and if the current 3 irradiance sensors in the albedometer are sufficient or whether there are more sensors required.

The report is structured in the following way. In Chapter 2 the solar irradiance, albedo, irradiance measurement devices and simulation models and the previous research done at the PVMD will be discussed. Then, Chapter 3 discusses how the SMARTS program simulates solar spectra, the methodology of the Spectrafy reconstruction model and the proposed method for the PVMD albedometer. Followed by Chapter 4 where the design of the reconstruction model, the required inputs and the results from initial tests with sensor data generated from SMARTS will be given. Next, in Chapter 5 the callibration of the albedometer with an EKO™ spectroradiometer will be discussed, followed by Chapter 6, where the results of the reconstruction model for 750 clear-sky measurements will be presented and analysed. Followed by the conclusion and recommendations for future research in the final chapter, Chapter 7.

2

Background

In this chapter an introduction to solar (spectral) irradiance will be given in Section 2.1, followed by the albedo in Section 2.2, existing measurement technologies in Section 2.3. Section 2.4 will discuss spectral simulation models and finally Section 2.5 wil discuss the previous research done at the PVMD.

2.1. Solar irradiance

Electromagnetic radiation from the sun, a product of the nuclear fusion within the sun, travels from the Sun to Earth, through the atmosphere to the surface. This radiation is the energy source for almost all processes on the surface of our planet (Smets et al., 2016). Plants convert incident radiation into oxygen and energy through photosynthesis, the radiation evaporates water which forms clouds and wind energy is a result of temperature differences in the atmosphere due to solar radiation. The solar radiation has different intensities at different wavelengths, usually described in units of $W/m^2/\mu m$ or $W/m^2/nm$. This intensity per wavelength is called the solar spectrum. The extra-terrestrial spectrum, or AM0 spectrum, is the solar spectrum that reaches the atmosphere. This spectrum is relatively constant, it only needs a correction factor for the ratio of the average to actual Sun-Earth distance, which changes due to the elliptical orbit of the earth around the sun. When the radiation passes through the atmosphere the spectrum is attenuated. An important factor in this attenuation is the length of the path that the radiation needs to travel through the atmosphere to reach a certain location on the surface. During sunrise and sunset the radiation has to travel further than in the middle of the day when the sun is at the vertical with the Earth, which results in a higher attenuation of the radiation. The angle of the sun with this vertical is called the zenith angle, Z. Figure 2.1 shows how the path of the solar radiation through the atmosphere varies for different zenith angles. AM is the air mass, $AM = \frac{1}{cos(Z)}$.

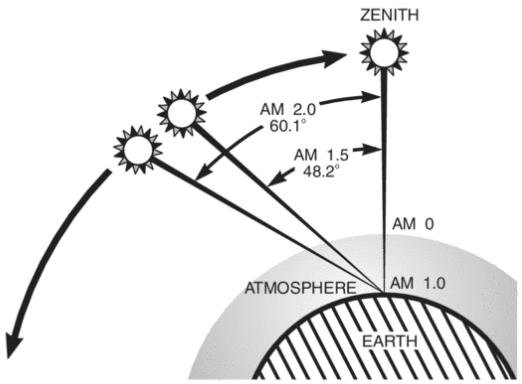


Figure 2.1: Path of solar radiation through atmosphere at different zenith angles (Fieducik, 2019)

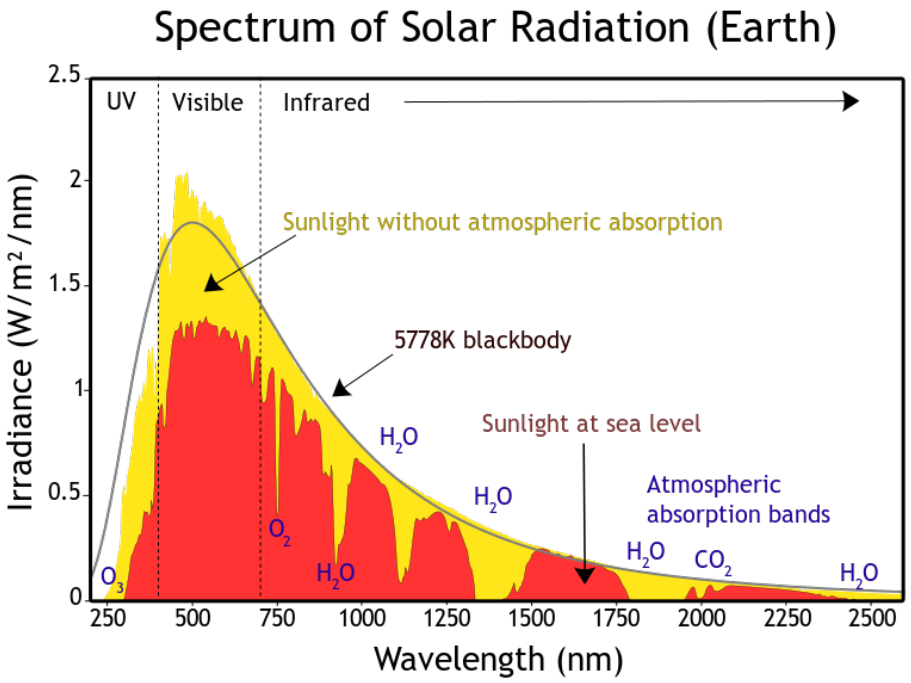


Figure 2.2: Extraterrestrial (AM0) solar spectrum and an example of the solar spectrum at sea-level (Rohde, 2013)

Besides the zenith, the composition of the atmosphere also attenuates the solar spectrum. Figure 2.2 shows the extra-terrestrial (AM0) spectrum in yellow and the spectrum at sea-level in red. Note that there are some wavelength bands where the AM0 spectrum is highly attenuated. This is caused by some gases that constitute the atmosphere. The red spectrum in Figure 2.2 is called the global horizontal irradiance (GHI). This GHI consists of 2 components, namely a direct (DNI) and a diffuse (DHI) component. DNI is the solar radiation arriving directly at the earth and DHI is the amount of solar radiation arriving indirectly, as clouds, water vapor, aorosols etc. reflect and absorb part of the radiation. The GHI as a function of wavelength λ is calculated with Equation 2.1 and Figure 2.3 shows the direct and diffuse component of the global irradiance, as well as the zenith angle mentioned before.

$$GHI(\lambda) = DNI(\lambda) * cos(Z) + DHI(\lambda) \tag{2.1}$$

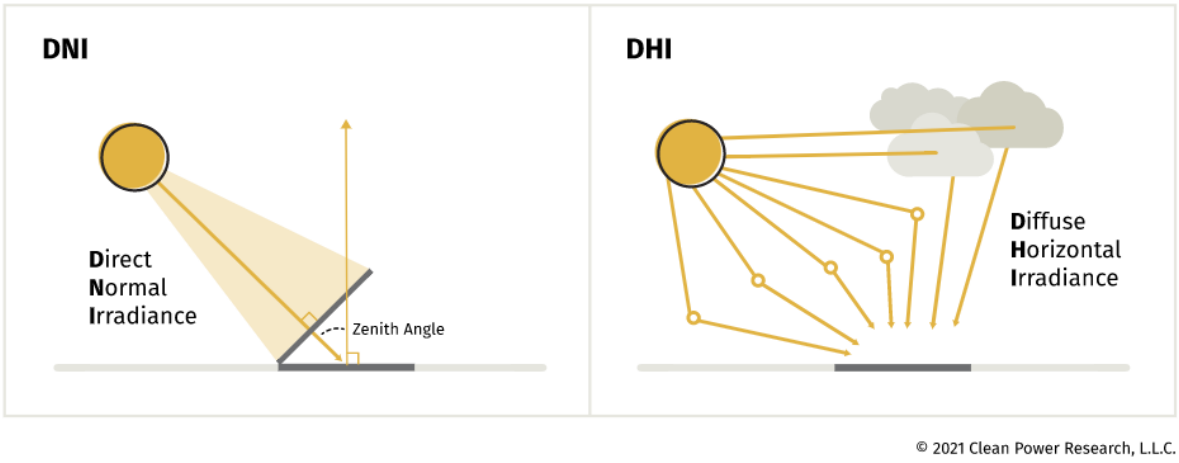


Figure 2.3: Direct and Diffuse component of Global irradiance (Solar Anywhere, 2021)

2.2. Albedo

As mentioned in the introduction, the albedo is the ratio between reflected irradiance and total irradiance. in Figure 2.4 it is shown that direct and diffuse sunlight reflects from the ground towards the back of the bifacial module. The performance of bifacial modules are highly dependent on the reflected irradiance, which can be as high as 25% of the incident irradiation on the front of module (Brennan et al., 2014). For vertically alligned PV modules the albedo is also an important influence on the energy yield. The albedo is spectrally and material dependent. Furthermore, it varies seasonally when the surface is covered in snow or the vegetation changes for example. Even during a day the albedo changes (Ziar et al., 2019). For example, after a rain shower there is water on the surface, which alters the albedo.

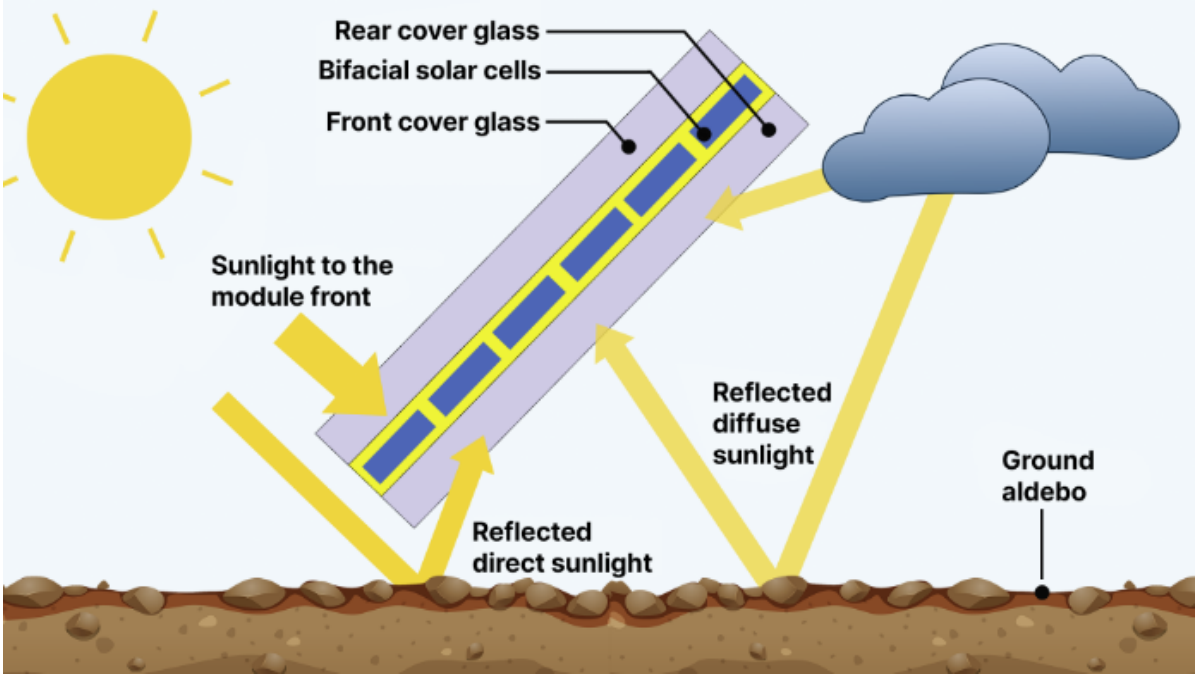


Figure 2.4: Bifacial module with reflected direct and diffuse irradiance due to the ground albedo (Sandhu, 2022))

Reference tables for spectral reflectivity exist, in SMARTS 65 are available and ECOSTRESS spectral library contains almost 3500 spectral reflectivities for different materials (Gueymard, 2008) (NASA, n.d.). The ECOSTRESS spectral library containts these reference tables can even be combined when the surroundings contain multiple surface materials. However, as the surroundings vary, especially in urban areas, the surroundings must be determined on a short-term basis. This requires a camera and someone classifying the surroundings.

2.3. Existing measurement technology

There are several devices available on the market that can measure irradiance in some manner, these devices can be divided into two categories, non-spectral devices that only measure the total irradiance and spectral measurement devices, which can measure the specific intensity of the radiation for different wavelengths.

2.3.1. Non-spectral measurement devices

Non-spectral measurement devices are devices that only give information about the total intensity of solar irradiances. Pyranometers measure the total GHI and are usually used to monitor performance of PV plants. Comparing the plants output with the pyranometer measurements determines the efficiency and drops in efficiency help to determine when the PV plant requires maintenance (Hukseflux, 2006). There are two types of pyranometers, thermopile pyranometers which absorb all thermal energy from the sun and converts it to electrical energy and semiconductor or silicon pyranometers which uses a photodiode to convert incoming light into current. The difference between the two is the wavelength

range that is measured. Silicon pyranometers only measure in the range of around 350-1100 nm, while thermopile pyranometers usually measure from 280 to 2800 nm (Institute, n.d.). Adding a shading mechanism to the pyranometer that blocks the direct irradiance component, now only the diffuse component is measured. Figure 2.5 shows a pyranometer to measure GHI and a pyranometer with a shading ring to measure DHI.
To measure the total albedo, two pyranometers can be assembled together, one facing upwards and one facing downwards. Another device is the pyrheliometer, which is used in combination with a sun-tracker to always be pointed directly towards the sun. This way, the direct component of the global irradiation is measured. Figure 2.6 Shows a pyrheliometer and an albedometer. These non-spectral devices are relatively cheap and thus relatively cost-effective to gain information about the irradiance at a PV site.



Figure 2.5: A pyranometer to measure global irradiance on the left and a pyranometer with added shading ring to measure diffuse irradiance on the right (Kipp & Zonen, n.d.)



Figure 2.6: A pyrheliometer to measure direct irradiance on the left and an albedometer on the right (Hukseflux, n.d.)

2.3.2. Spectral measurement devices

A spectroradiometer can be used to measure irradiance at different wavelengths, giving a more detailed view of the spectrum at a certain location. Since PV modules perform differently under different incident spectra, knowledge of the solar spectra at a location can be useful in determining why a PV site is not performing as expected and help in the design of a PV module for a specific location. Especially for multi-junction solar cells this the solar spectrum. Figure 2.7 shows the typical response of a triple-junction silicon solar cell (Smets et al., 2016) where 1,2 and 3 indicate the spectral response of the different junctions. When the actual spectrum deviates from the AM1.5 design spectrum, the performance of this solar cell can change significantly, as the worst performing junction determines the overall efficiency of the solar cell.

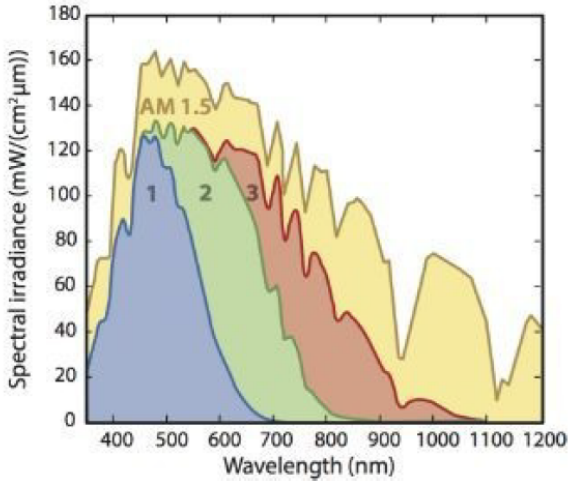


Figure 2.7: typical spectral utilization of a triple-junction thin-film silicon cell (Smets et al., 2016)

Figure 2.8 shows an EKO™ spectroradiometer of which the PVMD research group has two older versions (the MS-710). This spectroradiometer measures the intensity of incoming radiation for 256 wavelengths, in the range of 300-1100 nm. Two spectroradiometers can be combined to make a spectral albedometer, where one spectroradiometrer is facing upwards and one downwards. The cost of one EKO™ spectroradiometer is around €15.000,- (Kaul, 2020), significantly more expensive than the non-spectral measurement devices mentioned before and thus less used. Developing less expensive spectral devices can increase the usage of such devices. Ultimately this can increase world-wide spectral data and knowledge of the spectrum under different conditions.



Figure 2.8: EKO™ MS-711 Spectroradiometer (EKO, n.d.)

Spectrafy™

Spectrafy™, a company based in Ottawa and backed by research from the University of Ottawa, has designed spectral solar sensors that combine irradiance measurements with solar simulation software to reconstruct solar spectra for all weather conditions. In 2013 their first sensor was designed, which combines a multi-channel filtered radiometer with 6 channels with a reconstruction algorithm to obtain DNI spectra. Since then they have added a similar sensor (SolarSim-G) based on filtered photodiodes to measure and reconstruct spectra. Information on the placement and number of photodiodes is unavailable. The latest Spectafry addition is a spectral albedometer (SolarSim-Alb1), which uses two SolarSim-G back to back to not only determine spectral GHI, but also the reflected spectral irradiance at a location. These sensors are shown in Figure 2.9. The SolarSim-G and SolarSim-Alb1 are not as expensive as the EKO spectroradiometer(s), but the cost is still a 5-figure number.



Figure 2.9: From left to right: SolarSim-D2 spectral DNI, SolarSim-G spectral GHI and SolarSim-Alb1 spectral albedometer (Spectrafy, n.d.)

2.4. Spectral simulation models

Spectral simulation models, or solar radiative transfer models were developed to accurately simulate solar spectra. The basis of these models is to modify an extraterrestrial spectrum. As the extraterrestrial solar radiation moves through the atmosphere down to earth, atmospheric constituents absorb, transmit or scatter the solar radiation (Figure 2.2). To accurately simulate the solar spectrum, the mechanisms of absorption of these constituents must be described properly. Advanced spectral radiation models like MODTRAN, SBDART, COART and libRadtran, designed for atmospheric research, require specialized inputs and are relatively slow in execution due to their complexity (Gueymard, 2006). In the 80's a simplified model based on parameterizations to calculate spectral irradiance called SPCTRAL2 was developed. In the 90's a new Simple Model of the Atmospheric Radiative Transfer of Sunshine (SMARTS) was developed for clear-sky conditions, which improved the SPCTRAL2 model (Gueymard, 1993). Since then a new version of the program, SMARTS2 was developed (Gueymard, 2001), (Gueymard, 1995) and since then, has received some upgrades. In the remainder of this report, if SMARTS is mentioned, it refers to version 2.9.5.i13 from September 5, 2008 (Gueymard, 2008). SMARTS has now become the de facto spectral simulation standard in the solar community (Tatsiankou et al., 2014) and models like FARMS-NIT (Xie & Sengupta, 2019) (Xie et al., 2019) employ the SMARTS model and make efforts to improve or add functions, like a cloudy-sky model. Spectrafy™ also employs the equations and parameterized datasets from SMARTS (Tatsiankou et al., 2014). The SMARTS model will also be the starting point of the reconstruction model proposed in this thesis.

2.5. Previous research at the PVMD

In 2019, (Kaul, 2020) started the Master thesis project to design a cost-effective irradiance sensor for bi-facial PV applications. Bi-facial PV panels are PV panels that convert irradiance arriving at the front- and back-side of the PV panel. Knowledge about both the front and back irradiances is important to improve design of bifacial PV panels and also to imrpove the energy yield predictions. The final design of (Kaul, 2020) her thesis project was a prototype irradiance sensor that measures the irradiance in three wavelength bands, shown in Figure 2.10.

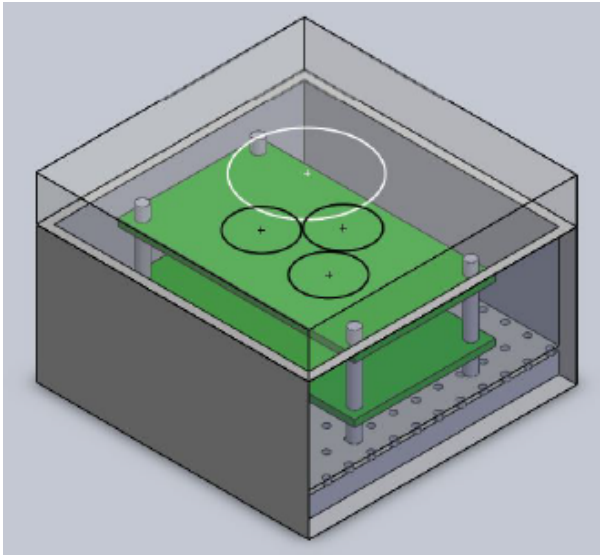


Figure 2.10: Irradiance sensor design by previous MSc. thesis project (Kaul, 2020). The white circle represents a light diffuser that diffuses all light equally to the 3 photo-diodes (black circles) below.

Next, (Romero Olvera, 2021) continued the work of (Kaul, 2020), improving the design of the diffuser and optical filters to obtain more accurate results. She designed an albedometer, shown in Figure 2.11, with a sensor facing upwards and one that faces downwards, in a cactus-inspired design that minimizes temperature effects within the albedometer. The final design measures the irradiance in three wavelength bands using three silicon photodiodes measuring wavelengths from 320 to 1100 nm and two commercial long-pass filters, one that attenuates irradiance below 900 nm and one that attenuates irradiance below 850 nm. Resulting in the measurement of irradiance in three wavelength regions: 320-1100 nm, 590-1100 nm and 850-1100 nm. From these measurements the irradiance in the wavelength regions of 320-590 and 590-850 nm can also be determined. The final albedometer design costs around €1.000,- (Romero Olvera, 2021). A factor 15 cheaper than the EKO™ spectroradiometer.



Figure 2.11: Albedometer design by previous MSc. thesis project (Romero Olvera, 2021). The cactus-inspired ribs minimize temperature effects within the sensor. The white diffuser on top diffuses the irradiance from all directions uniformly and the yellow level is used to position the albedometer horizontally.

3

Methodology

In this chapter the theory behind the SMARTS model will be discussed in Section 3.1. Section 3.2 discusses the reconstruction method from Spectrafy™ for the Direct Normal Irradiance and finally Section 3.3 discusses the proposed approach for the reconstruction model designed in this thesis project.

3.1. SMARTS

SMARTS determines the spectral irradiance is determined by modifying an extraterrestrial irradiance with parameterized transmittance and absorption functions for atmospheric constituents, which depend on its air mass and optical depth. The atmospheric constituents are divided into aerosol, water vapor, mixed gases, trace gases, ozone and Rayleigh transmittance (Gueymard & Myers, 2004). Rayleigh and aerosol scattering have an effect on the spectrum below 1500 nm, in Figure 2.2 it is clearly visible that the overall curve of the incident red spectrum is lower than the extraterrestrial yellow spectrum, whereas the two bands above 1500 nm are similar to the extraterrestrial spectrum. The peaks, or gaps, are caused by the other constituents, with water vapor the biggest contributor, causing the big peaks above 800 nm (except for some contribution of CO2 around 2000 nm). Ozone scatters irradiance below 350 nm. Mixed gases, such as oxygen and CO2 cause some minor peaks , located at 750 nm and 2000 nm for example. Trace gases are gases that have low concentrations in the atmosphere and only have a small effect on the spectrum. Although their effects can become high in below 700 nm when the air is highly polluted. Equations in this section are based on the equations from (Gueymard, 1993) (Gueymard, 1995), (Gueymard, 2001) and (Gueymard, 2008).

3.1.1. Direct Normal Irradiance

The direct component of the global irradiance, also called the direct beam radiation, is determined by multiplying the extraterrestrial irradiance (corrected for Sun-Earth distance) with transmittance functions for the atmospheric constituents, Equation 3.1.

$$DNI(\lambda) = Ex_{c\lambda} * T_{R\lambda} * T_{o\lambda} * T_{mg\lambda} * T_{tg\lambda} * T_{w\lambda} * T_{a\lambda} \tag{3.1}$$

where $Ex_{c\lambda}$ is the extraterrestrial spectral irradiance, corrected for the Sun-Earth distance, and $T_{R\lambda}$, $T_{o\lambda}$, $T_{mg\lambda}$, $T_{tg\lambda}$, $T_{w\lambda}$ and $T_{a\lambda}$ the Rayleigh, ozone, nitrogen, mixed gases, trace gases, water vapor and aerosol spectral transmittances respectively.
The principle equation behind all these transmittances is the Beer-Lambert-Bouguer law, that states that the transmittance of light is exponentially proportional to an absorption coefficient and the path-length it has to travel (Smets et al., 2016). For the transmittances from Equation 3.1 this is written as Equation 3.2.

$$T_{i\lambda} = exp(-m_i * \tau_{i\lambda}) \tag{3.2}$$

where m_i is the optical air mass of the constituents, which is dependent on the zenith angle. Each constituent has its own dependency on the zenith angle as their vertical concentration profile differ. $\tau_{i\lambda}$, the optical depth of each constituent depends on the concentration of the constituent in the

atmosphere, temperature, pressure and spectral absorption coefficients, which are derived from data from MODTRAN (see Section 2.4 (Gueymard, 2001).

Rayleigh transmittance

Rayleigh scattering is an approximation for electromagnetic scattering by particles much smaller than the wavelength of the incident radiation (Society, n.d.). When light interacts with this particles, photons are absorbed and scattered in different directions. Rayleigh scattering is inversely proportional to the fourth power of the wavelength, which means that light with smaller wavelengths is scattered much more efficiently. This causes the sky to appear blue, as blue light with a smaller wavelength is scattered much more than red light with a higher wavelength throughout the atmosphere (Optics, n.d.). Light that is scattered is cannot be transmitted. Thus the transmittance in the lower wavelength region is much lower than in the higher wavelength region, as can be seen in Figure 3.1.

The Rayleigh transmittance is calculated with Equation 3.3 following Equation 3.6

$$T_{R\lambda} = exp(-m_R * \tau_{R\lambda}) \tag{3.3}$$

with

$$\tau_{R\lambda} = \frac{Pr}{117.3405 * \lambda^4 - 1.5107 * \lambda^2 + 0.017535 - 8.7743E - 4 * \lambda^{-2}} \tag{3.4}$$

where Pr is the pressure ratio between actual pressure and sea-level pressure (101325 Pa). m_R is the Rayleigh optical air mass, which is a function of the zenith angle. The Rayleigh transmittance for solar irradiance can thus be described if the zenith angle and the pressure ratio are known. In Figure 3.1 the Rayleigh spectral transmittance for the monitoring station in Delft at 14:00 on March 8th modelled with SMARTS can be seen.

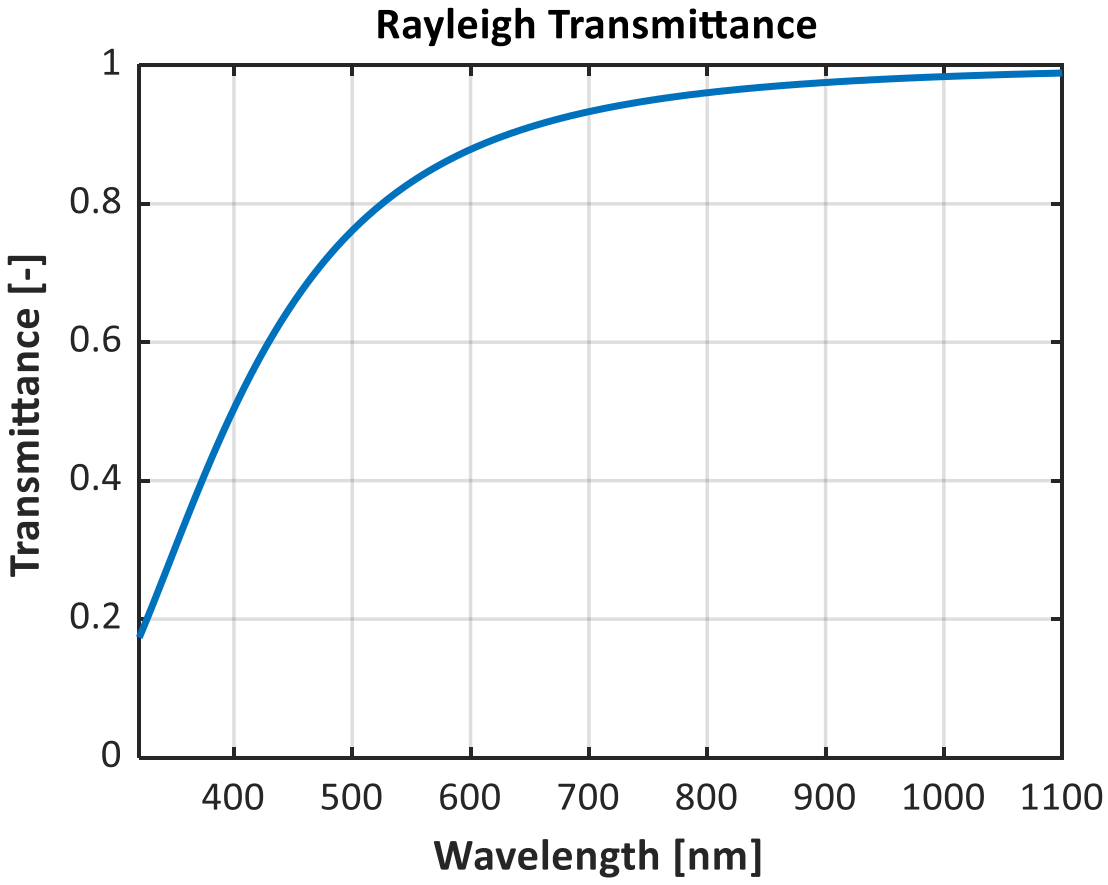


Figure 3.1: Rayleigh spectral transmittance for the monitoring station in Delft at 14:00 on March 8th modelled with SMARTS

Ozone transmittance

The ozone transmittance, caused by ozone particles in the atmosphere, is determined by Equation 3.5, which again follows Equation 3.2

$$T_{o\lambda} = exp(-m_0 * \tau_\lambda) \tag{3.5}$$

where m_0 is the ozone optical mass and τ_λ the ozone optical thickness, which is a function of u_o, the ozone reduced path-length (in atm-cm), temperature and 3 spectral coefficients. The ozone reduced path-length is the length of all ozone particles taken from a vertical path if they were brought down to earth to a pressure of 1 atm. To accurately describe the ozone spectral transmittance, the ozone reduced path-length, temperature and the zenith angle must be available. Figure 3.2 shows the ozone transmittance for the monitoring station in Delft modelled with SMARTS with u_o = 0.332 atm-cm, a value from the Mid-latitude summer reference atmosphere from SMARTS. The value for u_o should always be within [0, 1] atm-cm (Gueymard, 2008).

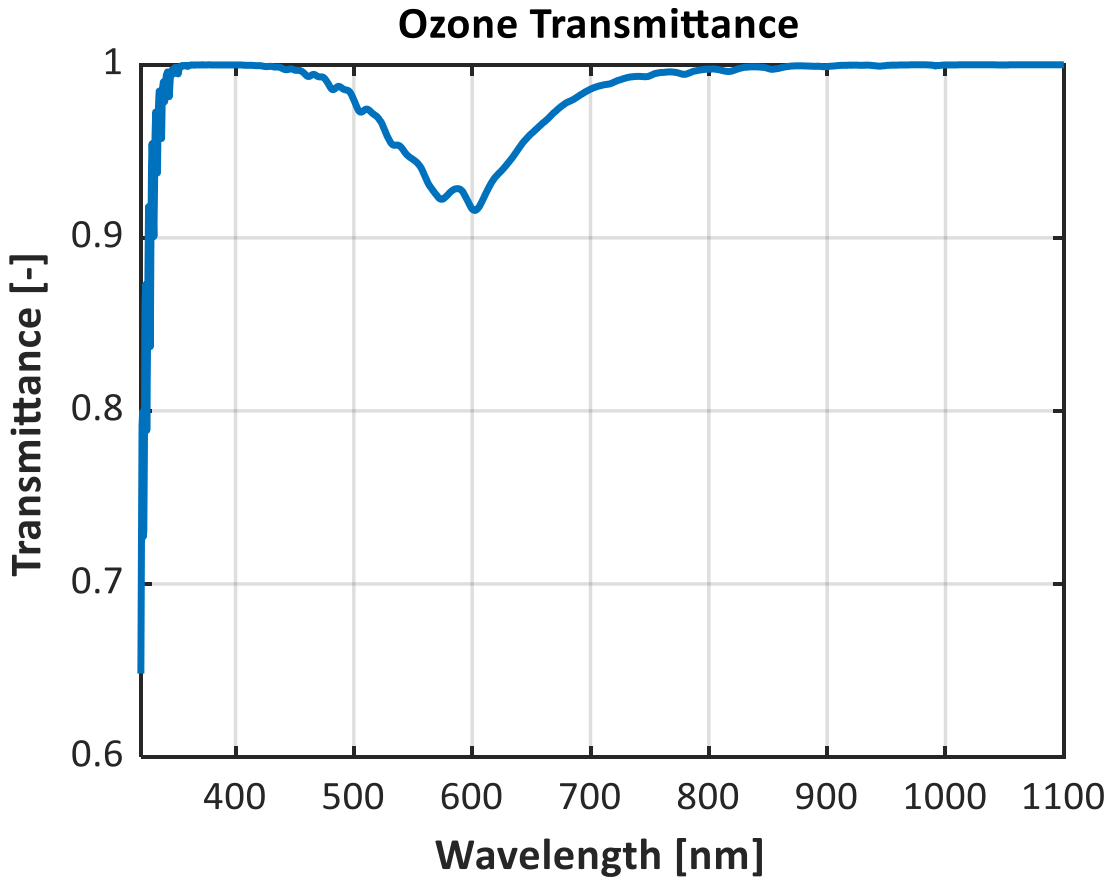


Figure 3.2: Ozone spectral transmittance for the monitoring station in Delft at 14:00 on March 8th modelled with SMARTS

Mixed & trace gases transmittance

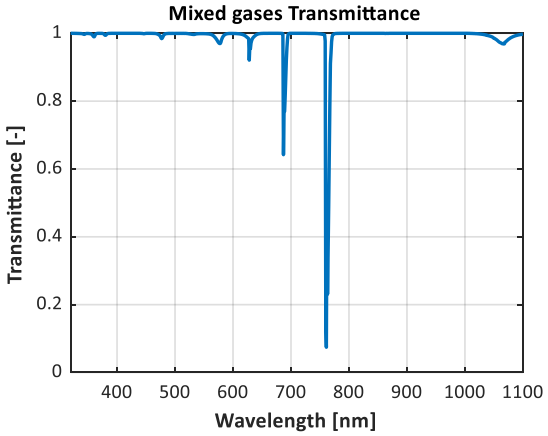
In the wavelength range of 320-1100 nm the mixed gases present are Nitrogen (N), oxygen (O_2), tetra-oxygen (O_4) and carbon dioxide (CO_2). Trace gases are nitric acid (HNO_3), nitrogen dioxide (NO_2), nitrogen trioxide (NO_3), sulfur dioxide (SO_2), bromine monoxide (BrO), formaldehyde (CH_2O), nitrous acid (HNO_2) and chlorine nitrate ($ClNO_3$). Mixed and trace gases are modeled following the Lambert-Beer-Bouguer law (Equation 3.2) with the optical depth, $\tau_{i\lambda}$, expressed in the constituents abundance Ab_i (in atm-cm) and spectral coefficient A_i in Equation 3.6. The gas abundances are corrected with temperature and pressure values and the spectral coefficient for each constituent is composed of multiple spectral coefficients with temperature or pressure corrections, or both. Figure 3.3a and Figure 3.3b show the mixed and trace gases transmittance for the monitoring station generated by SMARTS with gas abundance values from a reference atmosphere.

$$T_i = exp(-A_i * Ab_i * m_i) \tag{3.6}$$

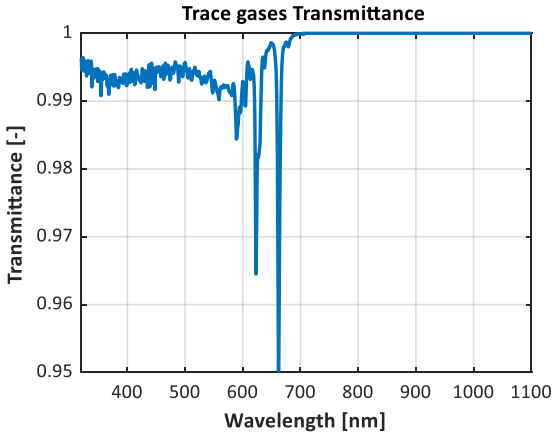
The total mixed gas transmittance is determined by Equation 3.7 and the trace gas transmittance by Equation 3.8

$$T_{mg\lambda} = T_N * T_{O_2} * T_{O_4} * T_{CO_2} \tag{3.7}$$

$$T_{tg\lambda} = T_{NO_2}. * T_{NO_3}. * T_{HNO_3}. * T_{SO_2}. * T_{BrO}. * T_{CH_2O}. * T_{HNO_2}. * T_{ClNO} \tag{3.8}$$



(a) Mixed gases spectral transmittance for the monitoring station in Delft at 14:00 on March 8th modelled with SMARTS



(b) Trace gases spectral transmittance for the monitoring station in Delft at 14:00 on March 8th modelled with SMARTS

Water vapor transmittance

Water vapor causes most of the peaks in the solar spectrum as shown in Figure 2.2. The higher the concentration of water, the greater the peaks in the spectrum. Water vapor transmittance is dependent on the total precipitable water, w in cm, its optical mass m_{H_2O}, and 16 spectral coefficients. These spectral coefficients modify different parts of the water vapor transmittance. Some of the coefficients modify for example the optical mass while others modify the total precipitable water. Figure 3.4 shows the water vapor transmittance with a w value of 2.922 cm at the monitoring station generated by SMARTS. The total precipitable water is within the following range: [0, 12] (Gueymard, 2008).

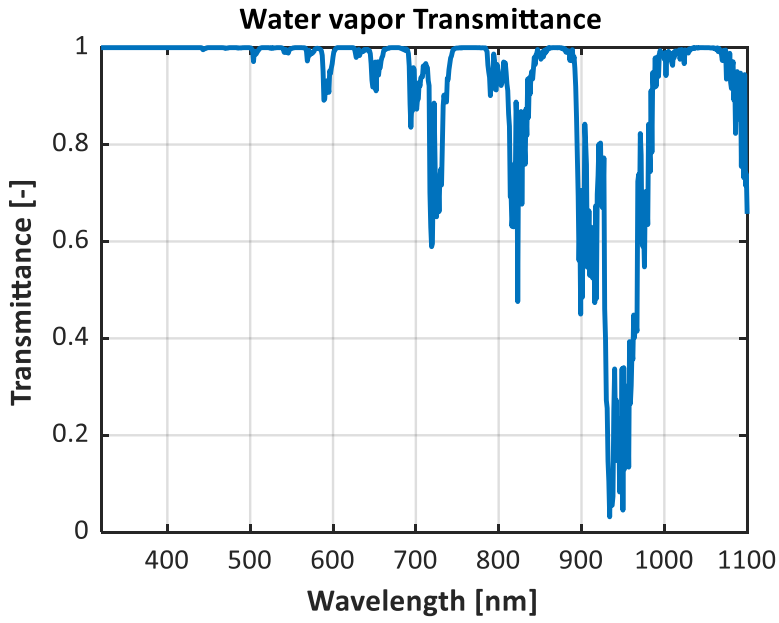


Figure 3.4: Water vapor spectral transmittance for the monitoring station in Delft at 14:00 on March 8th modelled with SMARTS

Aerosol transmittance

The aerosol transmittance is determined with the aerosol optical mass m_a and the aerosol optical thickness $\tau_{a\lambda}$, (Equation 3.10), in Equation 3.9

$$T_{a\lambda} = exp(-m_a * \tau_{a\lambda}) \tag{3.9}$$

$$\tau_{a\lambda} = \frac{\beta_i}{\lambda^{\alpha_i}} \tag{3.10}$$

where β and α are the Angström turbidity coefficient and the Ängstrom exponent respectively. aerosol optical depth is assumed to be linear on a log-log scale versus the wavelength, where a determines the slope of the curve and β is directly proportional to the aerosol optical depth (Bird, 1984). SMARTS has adjusted the modified Angström approach by (Bird, 1984), which considers 2 different spectral regions, above 500 nm ($\alpha_i = \alpha_2, \beta_i = \beta_2$) and below 500 nm ($\alpha_i = \alpha_1, \beta_i = \beta_1 = \beta_2 * 2^{\alpha_2 - \alpha_1}$). SMARTS determines α_1 and α_2 with different functions dependent on the relative humidity. These exponents are then modified with τ_{550}, the aerosol optical depth at a wavelength of 550 nm, which SMARTS converges to τ_{500} using the α_2 exponent derived from the relative humidity. β_2 is than calculated with a function dependent on α_2 and τ_{550}. The aerosol transmittance with τ_{550} = 0.0738 generated by the mid-latitude summer reference spectrum from SMARTS is shown in Figure 3.5, where the clear change in curvature above and below 500 nm can be seen. The aerosol optical depth is always in the range [0, 5] (Gueymard, 2008).

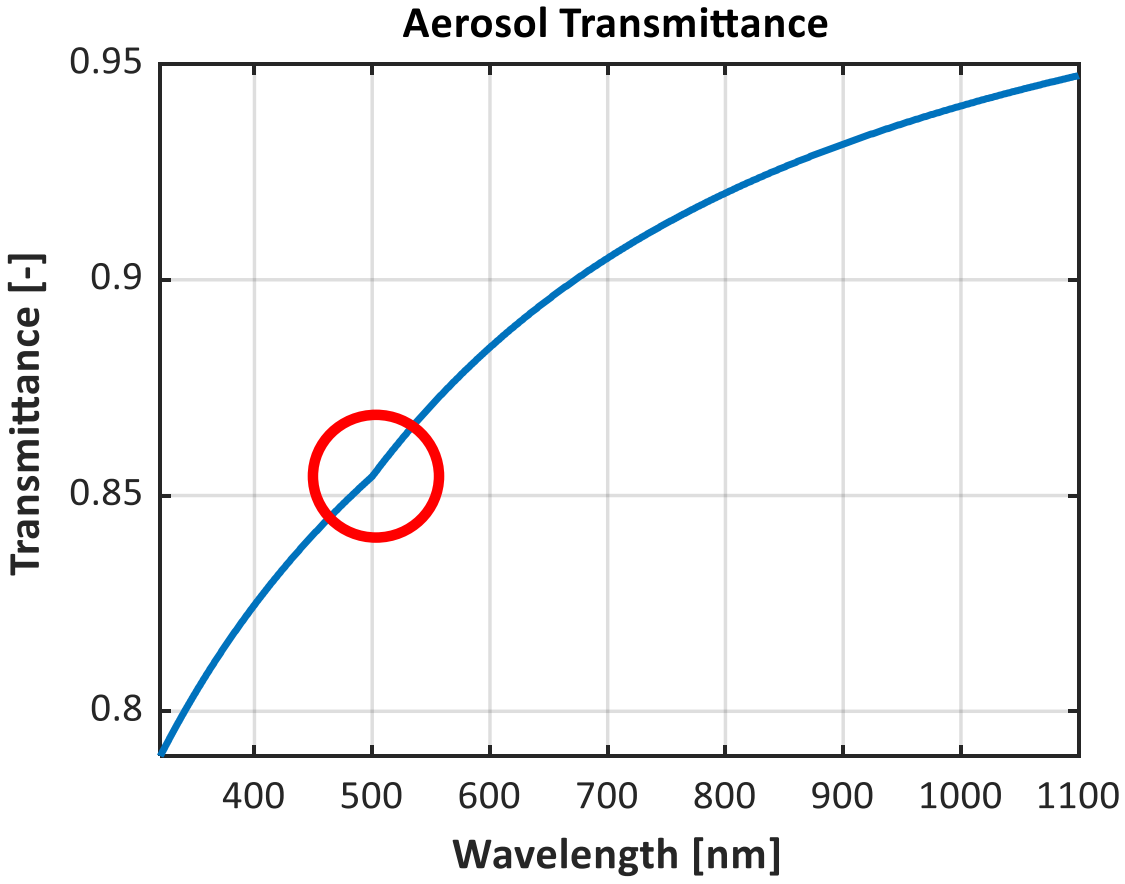


Figure 3.5: Aerosol spectral transmittance for the monitoring station in Delft at 14:00 on March 8th modelled with SMARTS, with the change in curvature below and above 500 nm is indicated with the red circle

3.1.2. Diffuse Horizontal Irradiance

The second part of Equation 2.1, the DHI, consists of three components: The Rayleigh scattered component, the aerosol scattered component and the back-scattered component. The DHI is calculated with modified equations from the DNI calculations. Where Rayleigh and aerosol scattering caused the DNI to attenuate, for the DHI component it is the irradiance scattered towards the measurement point from all directions. The backscattered component is modelled assuming infinite interreflections between ground and atmosphere. In this part, an additional parameter is introduced; the ground spectral reflectance, which determines the intensity of the reflected irradiance for each wavelength. In SMARTS, a pre-set reflectance can be chosen, for example soil, brick or roof tiles. The overall DHI is then determined following Equation 3.11, with $DHI_{R\lambda}$ the Rayleigh component, $DHI_{a\lambda}$ the aerosol component and $DHI_{b\lambda}$ the backscattered component.

$$DHI_\lambda = DHI_{R\lambda} + DHI_{a\lambda} + DHI_{b\lambda} \tag{3.11}$$

3.2. Spectrafy™ method

Spectrafy™ started with a reconstruction model with sensor input for DNI only (Tatsiankou et al., 2014). The equations behind follow the procedure of subsection 3.1.1, although they do not consider or mention the trace gas transmittances, which were also not mentioned in the original SMARTS model (Gueymard, 2001), but are incorporated into the updated SMARTS program (Gueymard, 2008). The trace gas transmittance could have been left out due to the fact that the effect on the spectrum is small under normal conditions (Figure 3.3b) or simply because the SMARTS paper did not mention it. Their approach was to measure irradiance for several narrow wavelength bands with a combination of interference filters and photodiodes in a so-called Multi-Channel Filter Radiometer (MCFR). They strategically chose the wavelength bands to isolate regions where only one unknown atmospheric parameter is present of the following: total preciptable water w in cm, ozone reduced-path-length u_o in atm-cm and the effect of aerosols. These parameters are chosen as SMARTS can accurately simulate spectra compared to spectroradiometer measurements if these parameters are known (Gueymard & Myers, 2004). The mixed gases and trace gases are more constant throughtout the atmosphere and have less of an effect on the total transmittance (Gueymard, 1995). Spectrafy™ uses 6 sensors, of which four are placed in regions where there is no water vapour or ozone effect to determine three sets of Ängstrom wavelength exponents and turbidity coefficients for the aerosol transmittance. The optimal position of these sensors are 420, 500, 780 and 1050 nm. After the aerosol transmission is determined the ozone and water vapour transmission can be determined with the two remaining sensors. One for ozone, placed at 610 nm, and one for water vapor at 940 nm. Figure 3.6 shows the wavelength regions where ozone and water vapour have an effect on the transmission. Aerosol channels must be placed outside these regions. A comparison between reconstructed and 46,454 measured spectra over a period of 2 years resulted in a RMS error of under 1.5% over 96% of the 350-1830 nm range for all-weather conditions (Tatsiankou et al., 2014). So although SMARTS is designed for clear-sky spectra only, with this approach other sky conditions can be reconstructed as well.

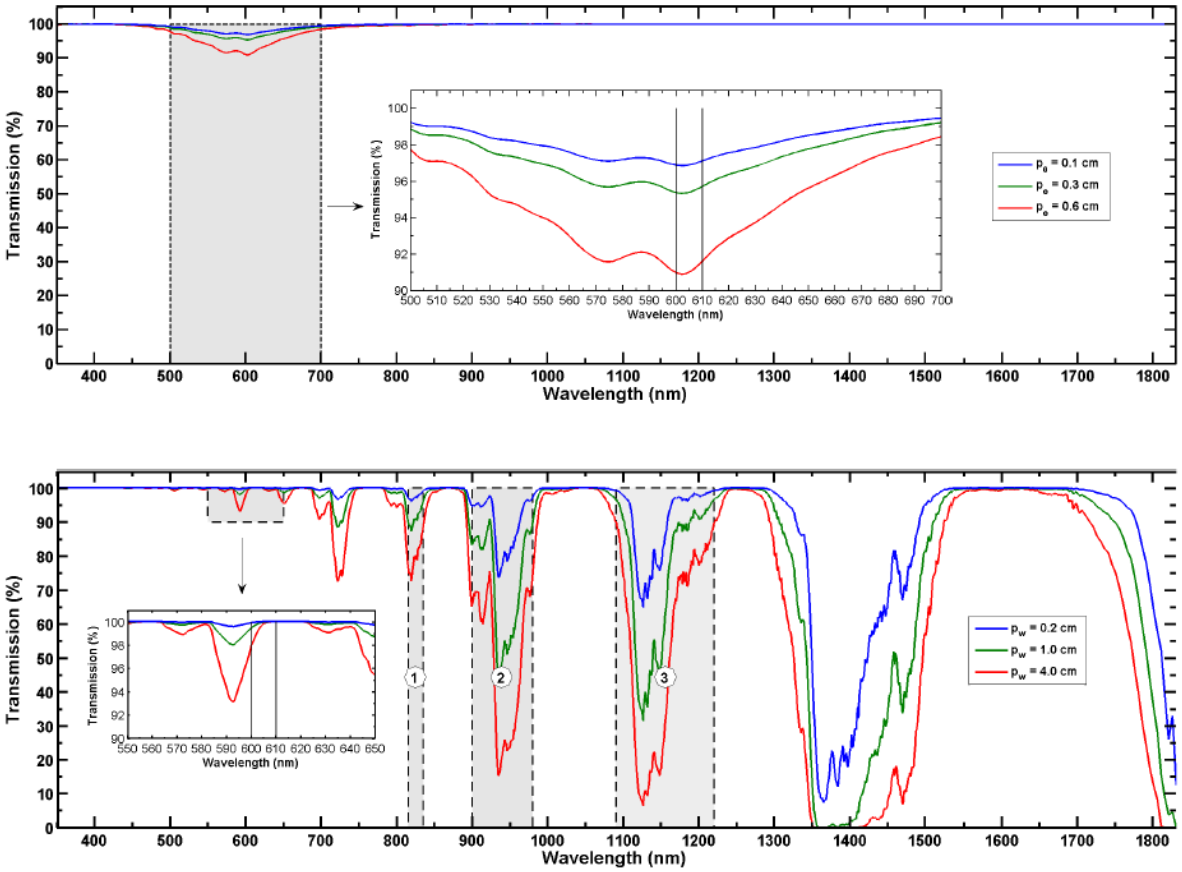


Figure 3.6: Ozone (top) and water vapour (bottom) transmittances from (Tatsiankou et al., 2014) which indicate possible placements of irradiance sensors to determine ozone reduced path-length u_o (p_w in figure) and precipitable water w (p_w in figure).

3.3. PVMD albedometer approach

As mentioned in Chapter 2, the PVMD albedometer provides irradiance data for the ranges 320-590, 590-850 and 850-1100 nm. In these ranges there is always an effect of water vapour or ozone transmission, thus it is not possible to isolate the aerosol, water vapour and ozone transmission in these wavelength ranges, so the same approach as Spectrafy™ cannot be applied to the albedometer sensor. Moreover the Spectrafy™ paper only reconstructs the DNI component of the irradiance. For the GHI there is an additional parameter that is unknown, namely the albedo. Therefore the following approach is proposed: The SMARTS model (for the 320-1100 range) is translated to MATLAB code. In order to simulate spectra, the following parameters must be determined: Aerosol optical depth at 550 nm, τ_{550}, the relative humidity (%), the ozone reduced path-length, u_o (atm-cm) and the total precipitable water, w (cm).A Particle Swarm Optimization algorithm will be used to find values for these parameters such that the difference between the simulated spectra and the albedometer measurements is minimized. Figure 3.7 shows a diagram of the reconstruction approach. In Chapter 4 the reconstruction model will be explained in more detail.

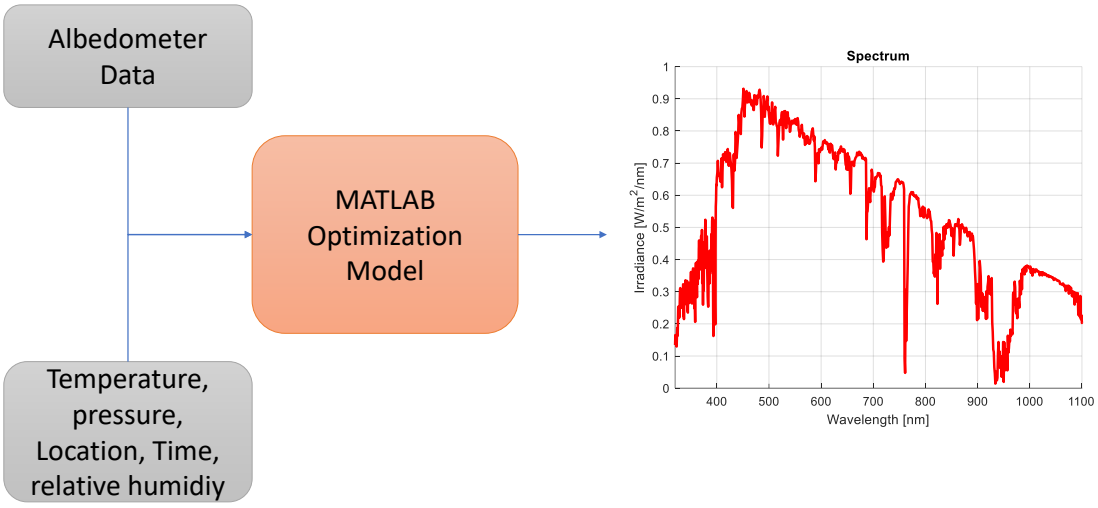


Figure 3.7: Reconstruction Approach, note that the relative humidity is also an input, and not an optimization parameter.

4

Design of reconstruction model

In this chapter the design of the reconstruction model will be discussed. In Section 4.1 the Particle Swarm Optimization will be discussed, followed by the assumptions and limitations of the current model in Section 4.2. Finally, the reconstruction results compared to SMARTS generated spectra at two timepoints will be presented in Section 4.3

4.1. Particle swarm optimization

The Particle Swarm Optimization (PSO) is an optimization algorithm to find a global minimum of a function. It is inspired by the behaviour of a flock of birds that searches for food. While searching for food the flock communicates how much food they see and each bird changes its movement based on this communication. Each bird represents a particle, the flock the swarm and the communication is a function evaluation that the PSO aims to minimize. For a function with n unknown parameters with lower and upper bounds, the PSO creates an n-dimensional space and disperses the particles equally over this space. For each iteration, the movement of each particle in the created space depends on 3 components, the inertia component, the individual best and the swarm best. The inertia component is the direction in which the particle moved in the previous iteration, the individual best is the direction at which the function evaluation was lowest for the particle, and the swarm best is the direction towards the lowest function evaluation of all particles for all previous iteration (Tam, 2021). These components are shown in Figure 4.1 on the left. These components are now combined to determine the movement of the particle in the next iteration, the new direction in the right part of Figure 4.1.

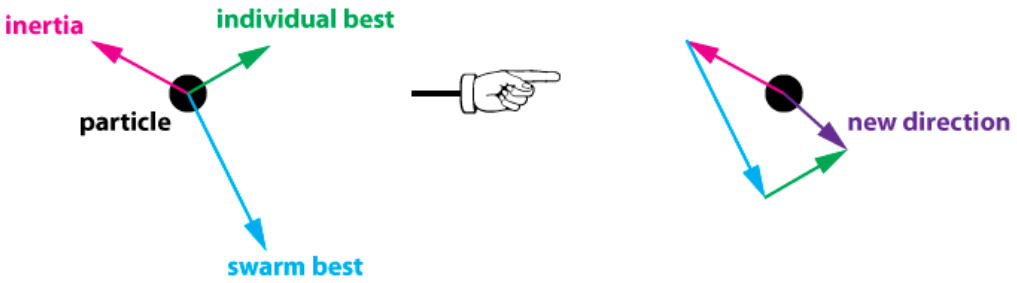


Figure 4.1: Movement of a particle in the PSO between iterations. (Adyatama, 2019)

The reconstruction model implements such a PSO, where the unknown or optimization parameters are the parameters that are not measured, but required for the accurate simulation of a spectrum in

SMARTS. Each particle then simulates a spectrum with the MATLAB adapted SMARTS clear skies model. These simulated spectra are compared to the irradiance data obtained from the albedometer. After the PSO converges to a minimum, the corresponding best values of the optimization parameters are given as output and the corresponding spectrum can be obtained. Figure 4.2 shows a schematic of the optimization path for the reconstruction model, the optimization variables and the error function will be discussed further in the subsections below.

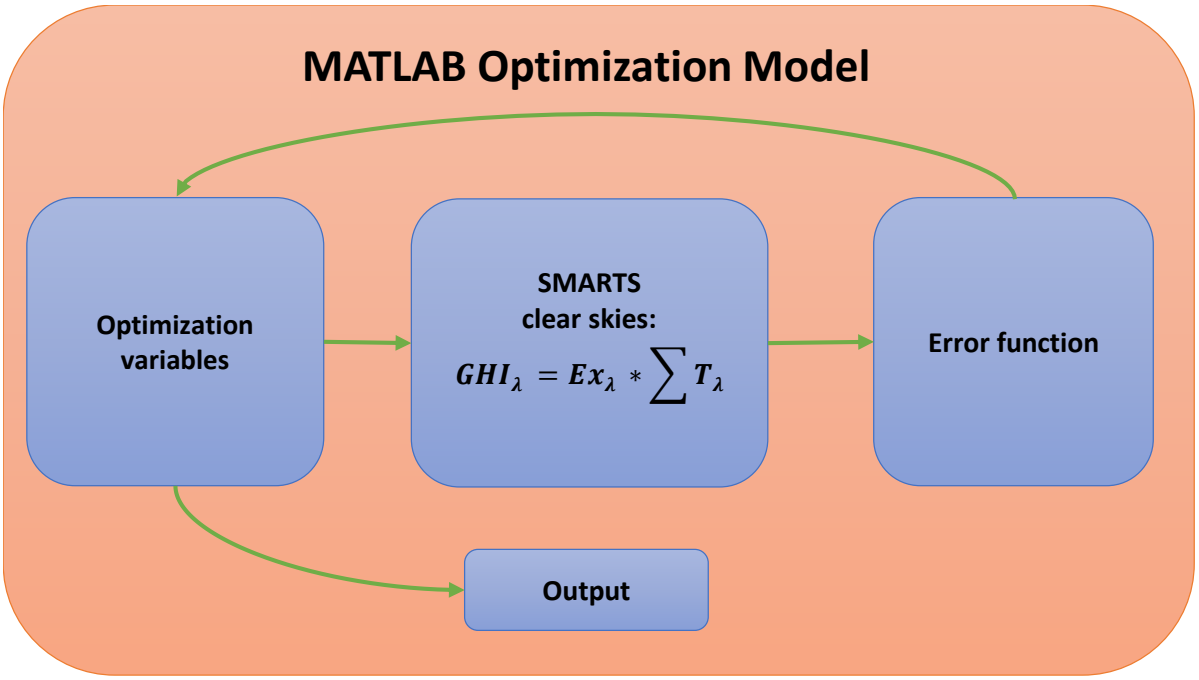


Figure 4.2: Diagram of the optimization model designed for the reconstruction of solar spectra. During each iteration the position of the particles change in the generated space, thus changing the optimization variables, which are evaluated by the spectral irradiance model, evaluated by the error function and based on this evaluation the position of the particles is adjusted again. When the position of particles are converged the optimization will output the best values for the optimization variables.

4.1.1. Input parameters

The input parameters for the reconstruction model are divided into two categories, firstly the parameters that are required in order to simulate a spectrum and secondly the reference irradiance parameters, obtained or derived from the albedometer measured data. These reference irradiance parameters are used in the error function of the PSO to compare the spectra generated by the PSO particles with the measured data from the actual spectrum.

The simulation parameter inputs:

- The albedo in the three smaller wavelength regions (320-590, 590-850 and 850-1100 nm), determined by dividing the bottom with the top irradiance values obtained from the albedometer.
- Temperature and relative humidity data. Temperature and humidity sensors are currently not integrated into the albedometer. They either have to be designed into the albedometer, or placed seperately. The relative humidiy was originally an optimization parameter, however initial tests with the reconstruction model resulted with inconsistent results. The relative humidity and the aerosol optical depth at 550 nm both influence the aerosol transmittance, which could result the model to have difficulties in finding the best value for these parameters. After changing the relative humidity to a measured variable the reconstruction proved to be more consistent.
- Pressure; a pressure sensor could be added, however in this thesis a constant value of 10200 Pa for the pressure for Delft is used, as pressure does not vary that much daily and is only used in the equations as ratio with the sea-level pressure. (Gueymard, 2008)

- The zenith angle, which is calculated with the pvl_spa function of PV_lib (PVPerformance, n.d.). For this, the latitude and longitude of the location are required.

The reference irradiance parameters

- GHI in 4 wavelength regions obtained from the albedometer (320-590, 590-850, 850-1100 and 320-1100 nm).
- DNI and DHI for the wavelength range of 320-1100 nm retrieved from the GHI data utilizing the BRL (Boland, Ridley and Lauret) decomposition model (Boland et al., 2013)(Ridley et al., 2010). The BRL model uses the ratio of GHI to the total extraterrestrial irradiance, the clearness index Kt, to estimate the diffuse fraction of the global irradiance. This total extraterrestrial irradiance is 1367 W/m^2. The GHI of the 320-1100 nm range is only a part of the entire spectrum, resulting in a lower extraterrestrial irradiance for this range of 1074 W/m^2 (Gueymard, 2008). Without adjusting the extraterrestrial irradiance, the clearness index is always underestimated resulting in inaccurate decompositions. Therefore the extraterrestrial irradiance was adjusted to this lower value. The BRL model had a decomposition error of 7 and -45 % for DNI and DHI respectively, achieving a better accuracy than the Reindl model (REINDL et al., 1990) which had errors of -31 and 125%.
  Initiall, decompositions in the ranges of 320-590, 590-850 and 850-1100 nm were also desired. However testing the errors of these compositions, again with adjusted extra-terrestrial irradiances for the wavelength ranges, resulted in significant errors, especially in the DHI values. This comparison is shown in Table 4.1. A further, more detailed investigation of the decomposition models was outside the scope of this thesis, thus it was decided to only use the decomposition for the 320-1100 nm range in order to minimize the effect of errors in the decomposition on the reconstruction model. The development of a more accurate decomposition model for the four different wavelength bands could provide the reconstruction with 12 more constraints. These 12 additional constraints could improve the accuracy of the reconstruction model.

Table 4.1: Decomposition test with Reindl and BRL decomposition model compared to SMARTS reference values for wavelength ranges 1,2 and 3 which are 320-590,590-850 and 850-1100 nm respectively

	SMARTS			**Reindl**			**BRL**		
Wavelength range	**1**	**2**	**3**	**1**	**2**	**3**	**1**	**2**	**3**
DNI [W/m^2]	261.9	263.7	324.4	304.4	251.4	119.8	324.4	265.6	125.1
DHI [W/m^2]	67.3	16.5	4.3	44.8	23.1	14.3	29.1	11.56	9.6
DNI error				**16%**	**-5%**	**-14%**	**24%**	**1%**	**-10%**
DHI error				**-33%**	**40%**	**231%**	**-57%**	**-30%**	**123%**

4.1.2. Optimization parameters

As discussed in Chapter 3, to accurately simulate solar spectra we need to have accurate values for the aerosol optical depth at 550 nm, τ_{550}, the relative humidity (%), the ozone reduced path-length, u_o (atm-cm) and the total precipitable water, w (cm). There are three parameters for the particle swarm optimization to determine. The parameters and their upper and lower limits are shown in Table 4.2

Table 4.2: Optimization parameters and their upper and lower limits (Gueymard, 2008)

Symbol	Name	Min	Max
τ_{550}	Aerosol optical depth at 550 nm (-)	0	5
u_o	Ozone reduced path-length (atm-cm)	0	1
w	totel precipitable water (cm)	0	12

4.1.3. Error function

The error function is the function that the particle swarm optimization tries to minimize. The 6 evaluation parameters mentioned in subsection 4.1.1 are the parameters that can be used to compare the spectra generated by the reconstruction model with the measurements from the albedometer. During each iteration of the optimization, the model simulates the values for these parameters from the spectra

generated by the particles in the swarm. The difference between the measured and reconstructed values are calculated and the error function is determined in Equation 4.1.

$$Error = a_1 * \left\| GHI^{diff}_{320-1100} \right\| + a_2 * \left\| DNI^{diff}_{320-1100} \right\| + a_3 * \left\| DHI^{diff}_{320-1100} \right\| + a_{11} * \left\| GHI^{diff}_{320-590} \right\| + a_{12} * \left\| GHI^{diff}_{590-850} \right\| + a_{13} * \left\| GHI^{diff}_{850-1100} \right\| \quad (4.1)$$

with $GHI^{diff}_{320-1100}$, $DNI^{diff}_{320-1100}$, $DHI^{diff}_{320-1100}$, $GHI^{diff}_{320-590}$, $GHI^{diff}_{590-850}$ and $GHI^{diff}_{850-1100}$ the differences between the reconstructed irradiance values and the measured values from the albedometer in the different wavelength ranges. The desired output of the reconstruction model is an accurate spectral GHI and in order to reduce negative effects of the imperfect BRL decomposition, weighting factors, a_i, are introduced to increase or decrease the fraction of the separate errors in the total error. There is no real mathematical procedure to determine the value of the weighting parameters, other than by trial and error. The weighting coefficients for the GHI components, a_1 a_{11} a_{12} and a_{13}, are set to 100, the weighting factor for the DNI, a_2, to 20 and the weighting factor for the DHI, a_3, to 10.

4.2. Assumptions and Limitations

The aim of the design of the reconstruction model was to keep it as simple as possible, to minimize computation time and to make it easier to locate possible problem areas in the reconstruction. The starting point was to only implement the original equations and spectral coefficients used by (Gueymard, 2001) and (Tatsiankou et al., 2014), however simulated spectra of the model deviated from the SMARTS reference spectra. Over the years SMARTS has updated and added spectral coefficients and these affect the spectrum. In order to implement these in our reconstruction model a significant part of the SMARTS source code was adapted to MATLAB code. Although SMARTS is called the ”Simple” model, the underlying code is quite elaborate and had to be translated from FORTRAN to MATLAB. It was decided to only implement the part of the code for the range of 320-1100 nm and that is valid for Delft and for horizontal irradiance calculations. Therefore the current reconstruction model is limited in its use. Further assumptions is that the air pressure is 10200 Pa and the CO2 concentration is 412.5 ppmv (NOAA, 2021). This value changes during the season and locally, but due to its limited effect, it only has an affect in the range of ≈1030-1180 nm (the utmost right peak in Figure 3.3a), it is assumed to be constant. The spectral reference albedo used in the SMARTS simulations is replaced by the less-spectral detailed albedo obtained from the albedometer sensor. The replacement of the spectral albedo with the average sensor albedos resulted in no differences in the reconstruction of the SMARTS spectra.

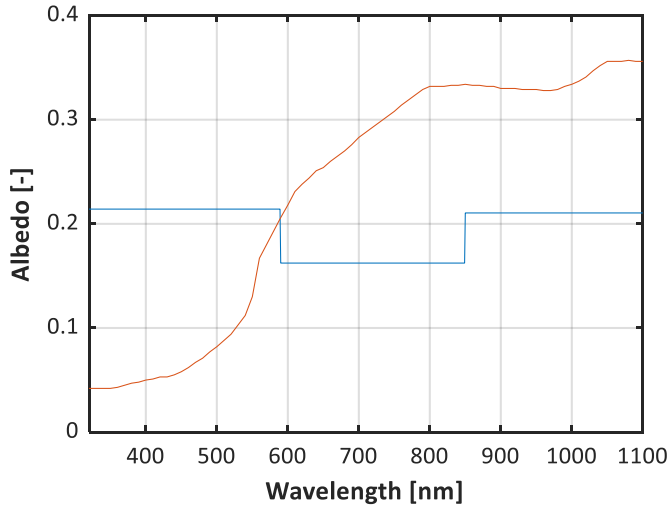


Figure 4.3: Spectral albedo in red compared to the albedo obtained from the sensors which is an average value across the three wavelength regions.

4.3. Reconstruction with respect to SMARTS spectra

The reconstruction model is initially tested with a SMARTS generated spectrum, to test if the model can accurately reproduce a spectrum without any influences of for example inaccurate measurement data. The reconstruction was tested with SMARTS generated irradiance values that represent the albedometer irradiance values. The model was tested for two different SMARTS spectra and for each it was run 20 times to ensure that the optimization parameters converge to the same value. In Figure 4.4 the results of this reconstruction test can be seen, where the reconstruction and the SMARTS reference spectrum is plotted at 8:00 on the left and at 14:00 on the right. These two times were selected to test the reconstruction for a high and a low zenith angle (83°at 8:00 and 58°at 14:00). The RMS errors are 0.005 and 0.0062 W/m^2/nm respectively. In Table 4.3 the values of the optimization parameters decided by the PSO algorithm are shown, together with an average run-time of the model for the 20 test runs. After initial tests where a single reconstruction took over 2 hours, the MATLAB code was optimized, which resulted in average computation times of around 147 seconds for the SMARTS generated spectrum at 8:00 and 98 seconds for the spectrum at 14:00.

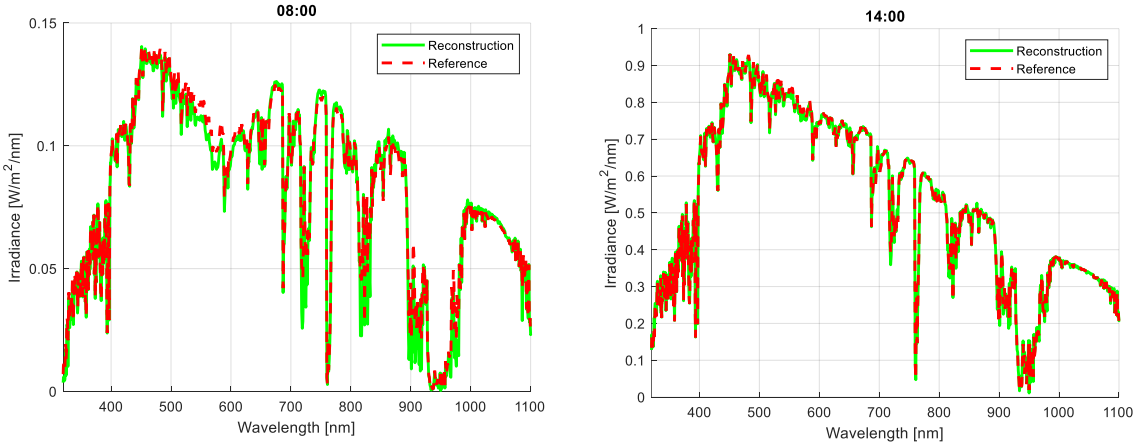


Figure 4.4: Reconstruction results compared two SMARTS generated spectra on March 8th at 8:00 on the left and at 14:00 on the right

Table 4.3: Optimization values obtained from the reconstruction model from tests with SMARTS generated spectra at 8:00 and 14:00 on March 8th

	tau_{550}	u_o	w	**Average runtime (s)**
SMARTS	0.073	0.332	2.922	
8:00	0.068	0.416	3.017	147
14:00	0.076	0.357	2.690	98

5

Measurement data and albedometer calibration

In the previous chapter it was proven that the model is able to reconstruct a spectrum generated from SMARTS. Now it must be tested with actual local measurements. These measurements are discussed in Section 5.1 the gathered data will be discussed, followed by the initial calibration in Section 5.2. An improved calibration is discussed in Section 5.3 followed by some remarks on the calibration process in Section 5.4.

5.1. Dataset

For the reconstruction model the following data is required: PVMD albedometer irradiance, temperature and relative humidity data. Furthermore, EKO™ spectroradiometer data is needed as a reference spectrum to assess the reconstructed spectrum. The albedometer records data every second and a dataset from March 8th to June 10th 2022 was obtained. The EKO™ spectroradiometer records spectral data every minute. The EKO™ and albedometer are installed at the PVMD monitoring station on a Solys 2 sun tracker, see Figure 5.1. The temperature and humidity sensors of the PVMD monitoring station were unfortunately not working, so there were no on-site measurements of the relative humidity and temperature. Relative humidity and temperature data was obtained via the Green Village, located nearby the PVMD monitoring station. Figure 5.2 shows the location of the PVMD monitoring station, circled in red, the location of the Green Village, circled in blue and the distance of around 700 meters, the black line.



Figure 5.1: Albedometer (circled in red) and EKO™ Spectroradiometer (circled in blue) installed at the PVMD monitoring station. They are installed on a Solys 2 sun-tracker. (Romero Olvera, 2021)

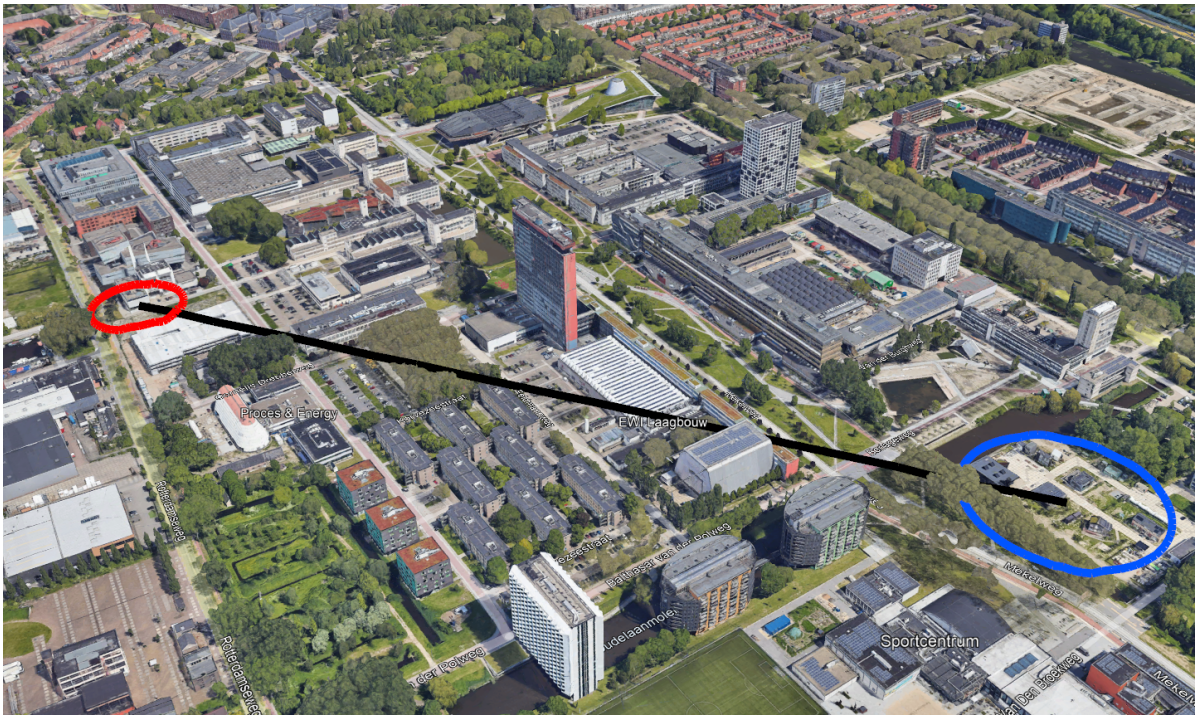


Figure 5.2: Location of the PVMD monitoring station, circled in red, the location of the Green Village, circled in blue and the distance of around 700 meters, the black line. The EWI building is located in the middle of the two.

5.2. Linear calibration

For the calibration of the albedometer irradiance sensors the recorded data was filtered first. The albedometer was calibrated with the EKO™ spectroradiometer, thus recorded data from the albedometer was matched to the EKO™ recorded spectral data. Furthermore, data-points with sun elevation angles below 30° were removed (elevation angle is equal to 90°minus the zenith angle). This reduced the dataset by 45%, 33317 data-points are left. A first correction to the albedometer data is the temperature correction factor of the photo-diodes, previously determined experimentally in the thesis of (Romero Olvera, 2021). The albedometer records data in μA and is temperature corrected according to Equation 5.1

$$I_{iTc} = I_i + k_i * (T - T_{ref}) \tag{5.1}$$

with I_{iTc} the temperature corrected current, in μA, for the three sensors (i = 1,2,3) . I_i is the current measured by the sensors, k_i the temperature correction factors which are -0.012, -0.108 and 0.054, in $\mu A/^{\circ}C$, for sensor 1, 2 and 3 respectively. T is the temperature measured within the albedometer and T_{ref} the temperature at which the coefficients were determined, 25 °C.

In order to use spectral data from the EKO™ spectroradiometer to calibrate the albedometer, the spectral data must be converted to representative sensor data. Firstly, the EKO™ spectral irradiance is wavelength matched to the albedometer sensor ranges. These ranges are 320-1100 nm, 590-1100 nm and 850-1100 nm. Secondly, the spectral matched data is integrated with respect to the wavelength with the trapezoidal method according to Equation 5.2.

$$EKO_{\lambda_{low}-\lambda_{high}} = \sum_{n=0}^{N-1} \frac{1}{2}(I_n + I_{n+1})(\Delta_\lambda)_n \tag{5.2}$$

with λ_{low} and λ_{high} the wavelength bounds, N the number of points, I_n the irradiance value at point n and δ_λ the wavelength interval between point n and $n-1$.
Next, the measured values from the albedometer for each sensor are compared to the representative values from the EKO™ spectroradiometer for all 33317 data-points. A first-degree polynomial least-squares fit is applied to calibrate the albedometer with the EKO spectroradiometer to obtain the coefficients a and b in the calibration function in Equation 5.3.

$$GHI_{alb} = a * I_{alb} \tag{5.3}$$

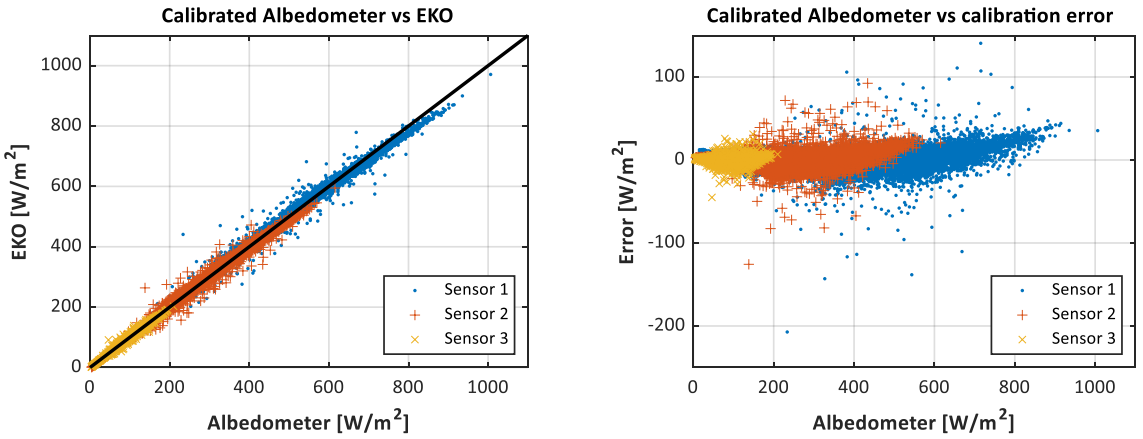
with a in $\frac{W}{\mu A * m^2}$, b in $\frac{W}{m^2}$, I_{alb} in μA and GHI_{alb} in $\frac{W}{m^2}$.
Table 5.1 shows the coefficients for the calibration function. After the calibration the relation of the calibrated albedometer against the EKO™ spectroradiometer reference data is shown in Figure 5.5a, where black line represents a perfect calibration. Deviations from this black line are calibration errors, which is shown in Figure 5.5b.

Table 5.1: Linear calibration of albedometer sensor data with the coefficients a and b for $y = ax + b$ where x is the temperature corrected current from the albedometer in μA.

Sensor	Wavelength range	$a[\frac{W}{\mu A * m^2}]$	$b[\frac{W}{m^2}]$
1	320-1100 nm	1.438	-13.129
2	590-1100 nm	1.133	-2.792
3	850-1100 nm	0.739	-3.675

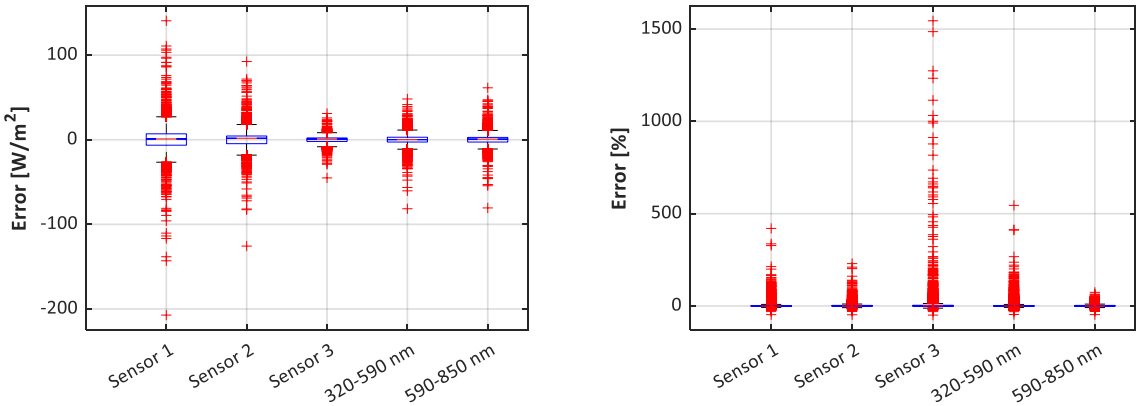
To quantify these calibration errors, box plots are made of the data set. A box plot is a figure that gives statistical information of the distribution of a data set by plotting the median, a box that contains 50% of the dataset, whiskers that indicate the 99.3% confidence interval if a normal distribution is assumed and the outliers (MathWorks, 2022). For the box plot a normal distribution of the calibration error is assumed. Besides box plots of the three sensors, box plots of the wavelength ranges 350-590 and 850-1100 are also determined. Figure 5.3a and Figure 5.3b show the box plots of the error in W/m^2 and % respectively. In these figures only the outliers of the data set are properly visible, the

red marks represent callibration errors that are outside the 99.3% confidence interval. Figure 5.4a and Figure 5.4b show the same figures, with the y-axis narrowed down to visualise the boxes and whiskers of the box plots. The blue boxes represent 50% of the data set . So 50% of the calibration errors are in within the limits of these boxes, with the red line the median of the data set. Adding the whiskers, the black dashed line with the horizontal black line tips, we now have a representation of 99.3% of the data set.



(a) (b) Calibrated albedometer sensor data vs calibration error

Figure 5.3: Calibrated albedometer sensors vs EKO™ spectroradiometer data in (a) and calibrated albedometer sensor data vs calibration error in (b)



(a) (b)

Figure 5.4: Box plot of calibration error of linear calibration of albedometer with EKO™ in W/m² in (a) and in % in (b)

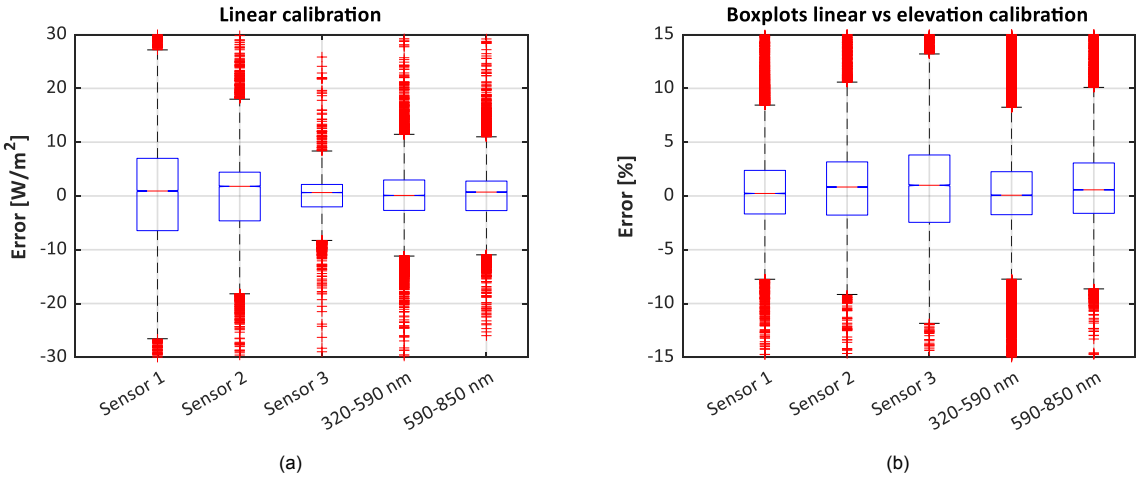


Figure 5.5: Zoomed box plot of calibration error of linear calibration of albedometer with EKO™, to better visualise the 99.3% confidence interval box in W/m^2 in (a) and in % in (b)

5.2.1. Clear Sky data calibration

For the reconstruction model an accurate calibration is desired, since the irradiance values are used in the reconstruction model to determine the much more detailed spectral irradiance. To improve the calibration, the data set of 33317 points is filtered with a clear-sky detector from PVLib (PVPerformance, n.d.), which uses a statistical analysis on short-term variations of the irradiance to detect clear-sky data-points. From the 33317 points, 6746 are classified as clear-sky data-points. Again, a 1-dimensional polynomial fit following Equation 5.3 is applied to the data set, which resulted in a new set of calibration coefficients, shown in Table 5.2.

Table 5.2: Linear calibration of albedometer sensor data with the coefficients a and b for Equation 5.3

Sensor	Wavelength range	$a[\frac{W}{\mu A * m^2}]$	$b[\frac{W}{m^2}]$
1	320-1100 nm	1.369	14.092
2	590-1100 nm	1.048	22.253
3	850-1100 nm	0.658	8.748

For the clear-sky calibrated dataset, the same analysis is done as for the entier data-set. Figure 5.6a shows the calibrated albedometer irradiance against the EKO™ irradiance values. It is clearly visible that compared to Figure 5.3a the data-points are closer to the perfect calibration line. In Figure 5.6b it can be noticed that the irradiance errors are now within -20 and 40 W/m^2, whereas in Figure 5.3b the range was approximately -200 to 150 W/m^2. Also the box plots in Figure 5.6a, Figure 5.6b, Figure 5.7a and Figure 5.7b are more centered closer to the zero error line.

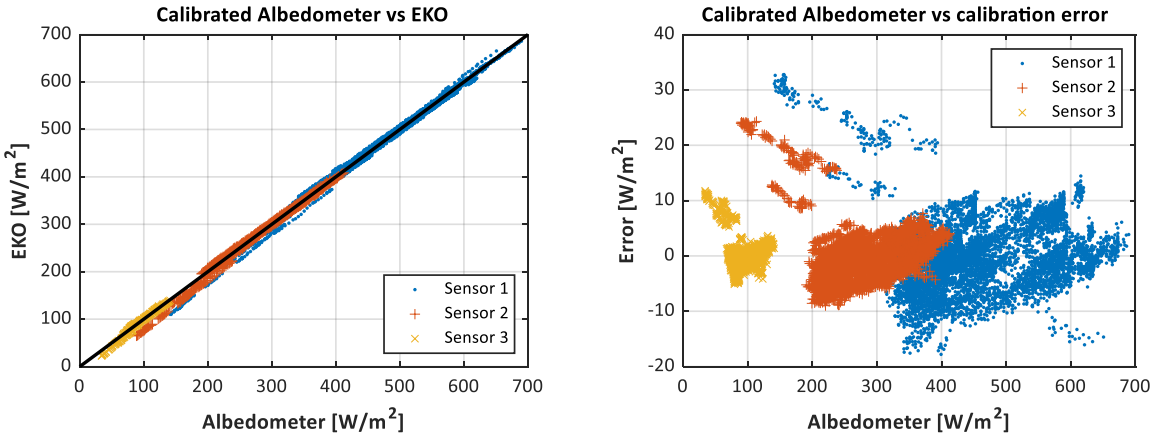


Figure 5.6: Calibrated albedometer sensor data vs EKO™ spectroradiometer data in (a) and calibrated albedometer sensor data vs calibration error in (b)

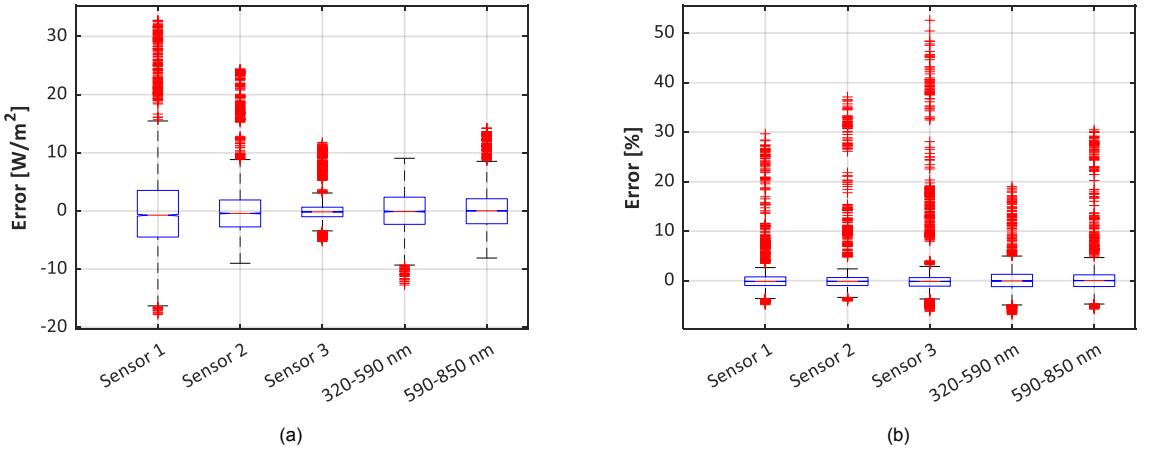


Figure 5.7: Box plot of calibration error of clear-sky linear calibration of albedometer with EKO™ in W/m^2 in (a) and in % in (b)

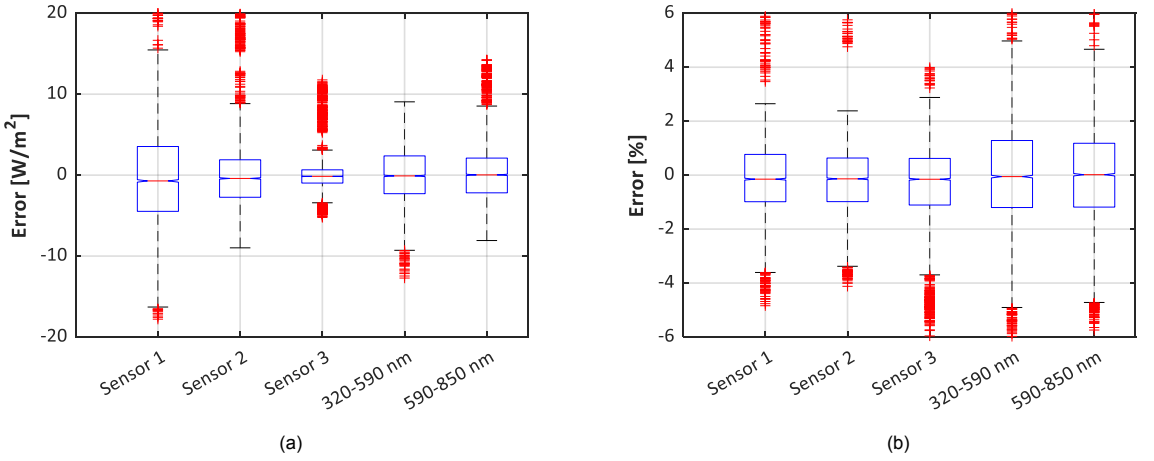


Figure 5.8: Zoomed box plot of calibration error of clear-sky linear calibration of albedometer with EKO™, to better visualise the 99.3% confidence interval box in W/m^2 in (a) and in % in (b)

5.3. Elevation angle adjustment

In an effort to find possible causes of the outliers, a relation between calibration errors and sun azimuth and elevation angles was investigated. The relation of the albedometer data I_{alb} (μA) divided by the EKO™ spectroradiometer data GHI_{EKO} (W/m^2) with the azimuth and elevation angles is shown in Figure 5.9. The relation with the elevation angle seems to follow a quadratic, or a second order polynomial, function. The azimuth does not appear to have a direct relation. Thus, a second order polynomial fit of the albedometer data divided by the EKO™ data is applied with respect to the elevation angle following Equation 5.4.

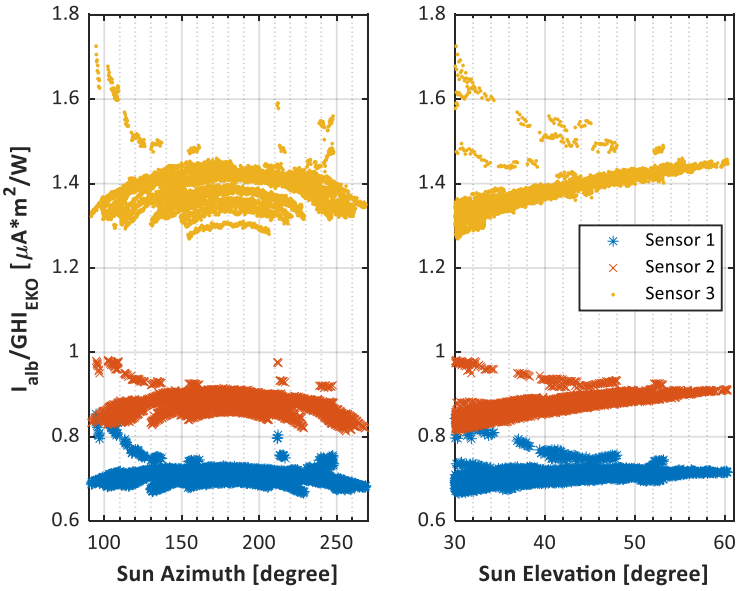


Figure 5.9: I_{alb}/GHI_{EKO} against azimuth and elevation angle for clear-sky data

$$y = a * El^2 + b * El + c \tag{5.4}$$

with El the elevation angle in °. a in $\frac{\mu A*m^2}{W*^{\circ 2}}$, b in $\frac{\mu A*m^2}{W*^{\circ}}$, c in $\frac{\mu A*m^2}{W}$ and y in $\frac{\mu A*m^2}{W}$. The values for a,b and c are shown in Table 5.3.

Table 5.3: Elevation calibration function of albedometer sensor data with the coefficients a, b and c for Equation 5.4

Sensor	Wavelength range	a[$\frac{\mu A*m^2}{W*^{\circ 2}}$]	b[$\frac{\mu A*m^2}{W*^{\circ}}$]	c[$\frac{\mu A*m^2}{W}$]
1	320-1100 nm	-1.2535e-05	0.0020	0.6490
2	590-1100 nm	-1.5477e-05	0.0035	0.7591
3	850-1100 nm	-9.0556e-05	0.0125	1.0185

In Figure 5.10 the resulting calibration factors are added to the figure. In the elevation figure on the right it can clearly be seen that the second order polynomial follows the paths of the sensors and the correction factors also appear to be similar in shape in the azimuth figure on the left. The calibrated albedometer irradiance is now determined by dividing the albedometer current with Equation 5.4. The relation with the azimuth and elevation angle after the calibration is shown in Figure 5.11.

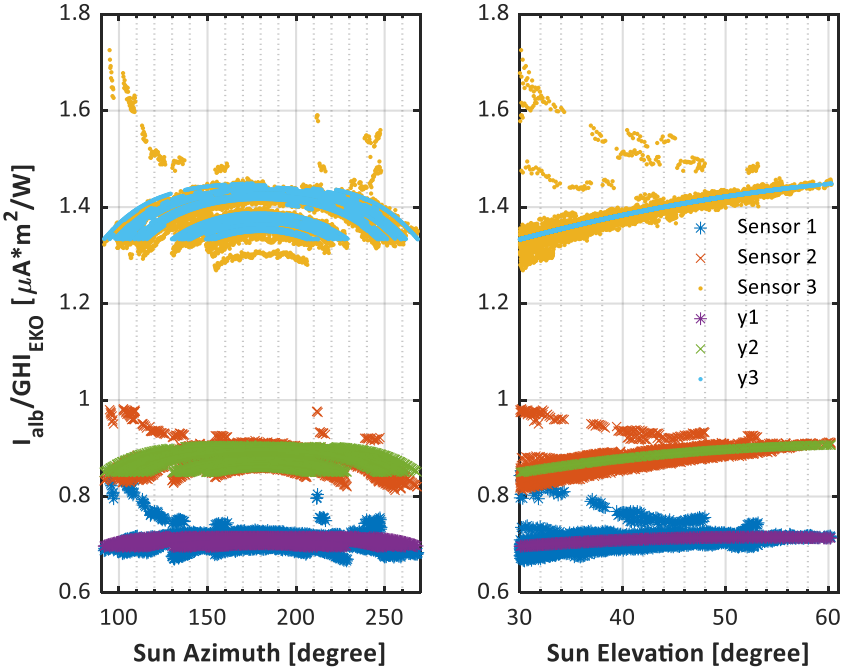


Figure 5.10: I_{alb}/GHI_{EKO} against azimuth and elevation angle for clear-sky data with the polynomial calibration functions y1,y2 and y3 added

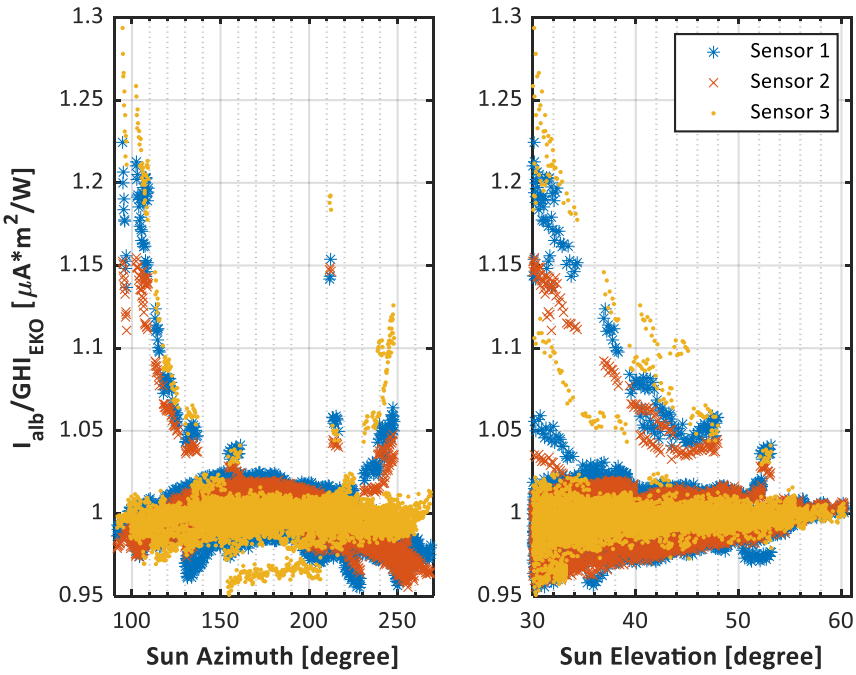
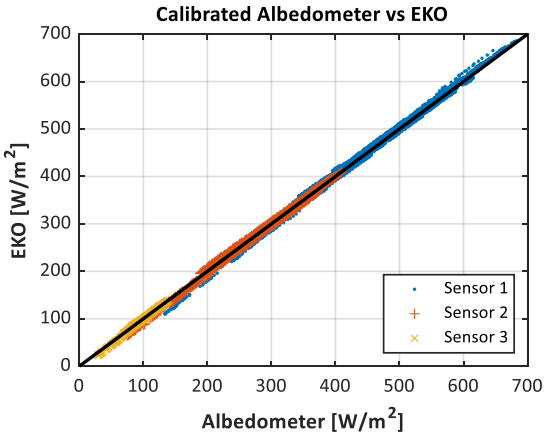
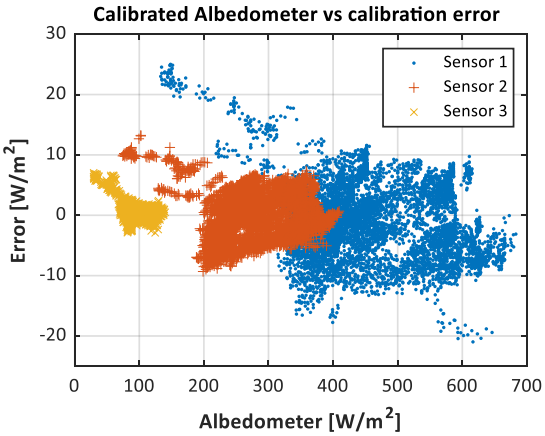


Figure 5.11: I_{alb}/GHI_{EKO} against azimuth and elevation angle for clear-sky data after the calibration

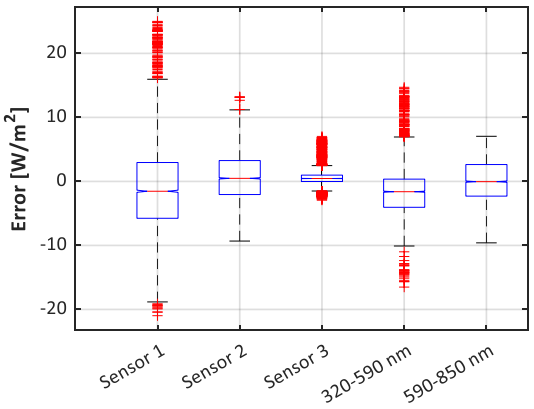
To compare this new calibration with the linear clear-sky calibration, the same analysis as with the linear calibration is done again for the clear-sky data. Figure 5.12a shows that the calibration is again close to the perfect calibration line. In Figure 5.12b the sensor errors seem more concentrated compared to Figure 5.8b although some of the errors in the bottom right of sensor 1 seem to have increased a bit in magnitude. Figure 5.13a, Figure 5.13b, Figure 5.14a and Figure 5.14b show that the overall accuracy of the calibration has improved, with the most significant change in the outliers of sensor 3 in Figure 5.13b, where it is reduced from around 50% to around 30%. Given the overall increased accuracy of this calibration method with respect to the elevation angle, it was decided to use the data from this calibration for the tests of the reconstruction model.



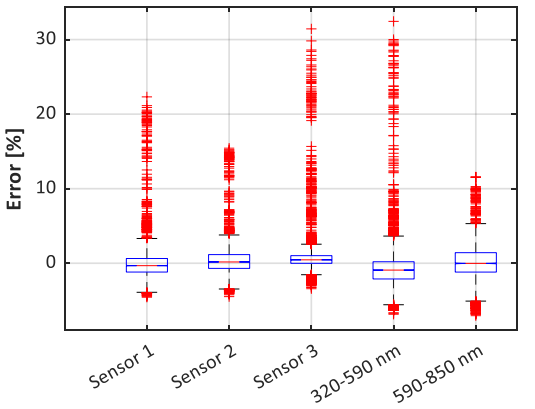
(a) Calibrated albedometer sensor vs EKO™ spectroradiometer



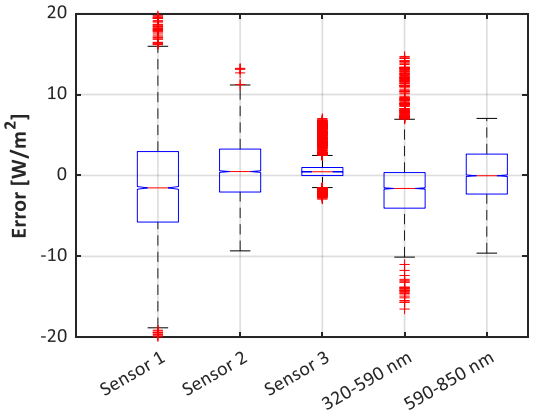
(b) Calibrated albedometer sensor data vs calibration error



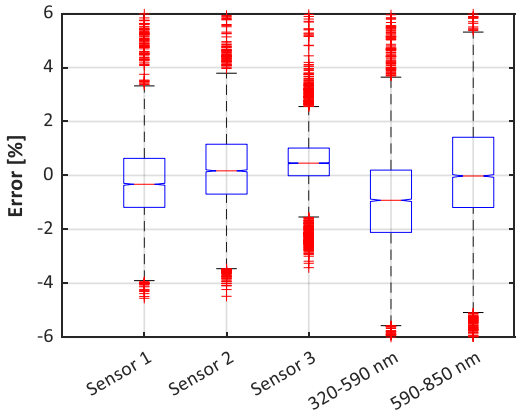
(a) Box plot of calibration error in W/m² of adjusted calibration of albedometer with EKO™



(b) Box plot of calibration error in % of adjusted calibration of albedometer with EKO™



(a) Zoomed box plot of calibration error in W/m² of adjusted calibration of albedometer with EKO™, to better visualise the 99.3% confidence interval box



(b) Zoomed box plot of calibration error in % of adjusted calibration of albedometer with EKO™, to better visualise the 99.3% confidence interval box

5.4. Remarks

The albedometer is calibrated using the EKO™ spectroradiometer. This spectroradiometer itself also requires calibration and has a measurement uncertainty. It was unknown when the spectroradiometer was calibrated for the last time, so a second spectroradiometer was sent to Japan to be calibrated. The calibration of the data-set has thus been done with an unknown calibration of the EKO™ spectroradiometer. Furthermore, after the replacement of the first spectroradiometer with the calibrated spectroradiometer it was discovered that the first spectroradiometer was not installed perfectly horizontal. This could potentially explain the relation that was found with respect to the elevation angle and could explain the fact that the calibration errors are not centered around zero. The errors not being centered around zero can indicate an imperfect calibration or that there still is some systematic error.

With the calibrated EKO™, some measurements were done and the calibration of the albedometer seemed to have been improved (although a much smaller data-set was used for this calibration. Unfortunately the spectra recorded with the EKO™ showed unexpected behaviour and after contact with the EKO™ it was concluded that the new data cannot be used until further investigation. EKO™ also shared a calibration certificate for the re-calibrated spectroradiometer, containing the uncertainty ranges of this new calibration, with the uncertainty being ±11.35%, ±5.00% and ±4.39% for the ranges of 350-450 nm, 450-900 nm and 900-1050 nm respectively. Since the calibration and uncertainty of the EKO™ used to obtain the data-set used, the uncertainty for the uncalibrated spectroradiometer is assumed to be similar as the re-calibrated one.

6

Reconstruction results & analysis

After the calibration of the albedometer, the reconstruction model is tested. Firstly, the calibrated albedometer data and EKO™ spectroradiometer data were matched with the relative humidity and temperature data obtained from the Green Village. Data-points where there is no recorded temperature or humidity values were removed. 5269 of the original 6746 clear-sky are left. With an average of 2 minutes per run from the initial tests (see Table 4.3) reconstructing all these points would take 176 hours. Therefore the data-set is reduced further with an interval of 5 minutes. Due to the fact that the data-points are under clear-sky conditions the spectrum is not expected to change significantly in 5 minutes. Therefore the data-set of 5 minutes should be a good overview of all the data-points.

To compare the reconstruction results with the EKO™ reference spectra, the reconstruction results must be interpolated to match the EKO™ wavelengths. The reconstruction simulates the spectra for wavelengths 320 to 400 nm with a 0.5 nm resolution, and between 400 and 1100 nm with a resolution of 1 nm. The EKO™ spectroradiometer measures the spectra with a resolution of ≈3.3 nm in the total range. The reconstruction resolution is thus downgraded and interpolated to match the wavelengths of the EKO™ spectroradiometer.

6.1. Reconstruction results

The reconstruction of the 1062 spectra took 16 hours and 15 minutes, which averages a little less than 1 minute per reconstruction. Figure 6.1 shows the reconstruction result for the data-point with the highest total irradiance in the 320-1100 nm wavelength range, 631 W/m^2. The reconstructed spectrum is close to the EKO™ measured spectrum for the range of around 520-1100 nm, however in the wavelength range of 320-520 nm the reconstruction deviates from the measured spectrum. This is also clearly visible in Figure 6.2a and Figure 6.2b where the reconstruction error with respect to the EKO™ measured data and its uncertainty range is plotted. In the range of 520-1100 the reconstruction error stays within the uncertainty range of the EKO™, apart from some peaks, for example the peak between 759 and 770 nm. This error is not necessarily a reconstruction error, but could also be caused by the difference in resolution of the reconstruction model and the EKO™ measured data or the consequent interpolation of the reconstruction data. Also in the region between 900 and 1000 nm, where the water vapor transmittance has its effect, the error is outside the uncertainty range of the EKO™. However in Figure 6.1 the reconstruction follows the shape of the EKO™, with some oscillations, which could again be caused by the difference in resolution. The errors in the range of 320-520 nm are however concerning. Besides the reconstruction being inaccurate in this wavelength range, due to the fact that the reconstruction model finds the optimization parameters by utilizing the errors in the range of 320-590, 590-850 and 850-1100 nm, a high error in one of the regions can cause the other regions to be less accurately reconstructed as well. In an effort to improve the reconstruction the weighting factors from Equation 4.1 were adapted to a_1 = 1, a_{11} = 1 a_{12} = 10,000, a_{13} = 100 and a_2 = 100. a_3 remained 10. The main idea was to reduce the weighting factor of the first wavelength range to minimize the effect this error has on the other parts of the spectrum. The results shown in Figure 6.1, Figure 6.2a and Figure 6.2b are already with these weighting factors applied.

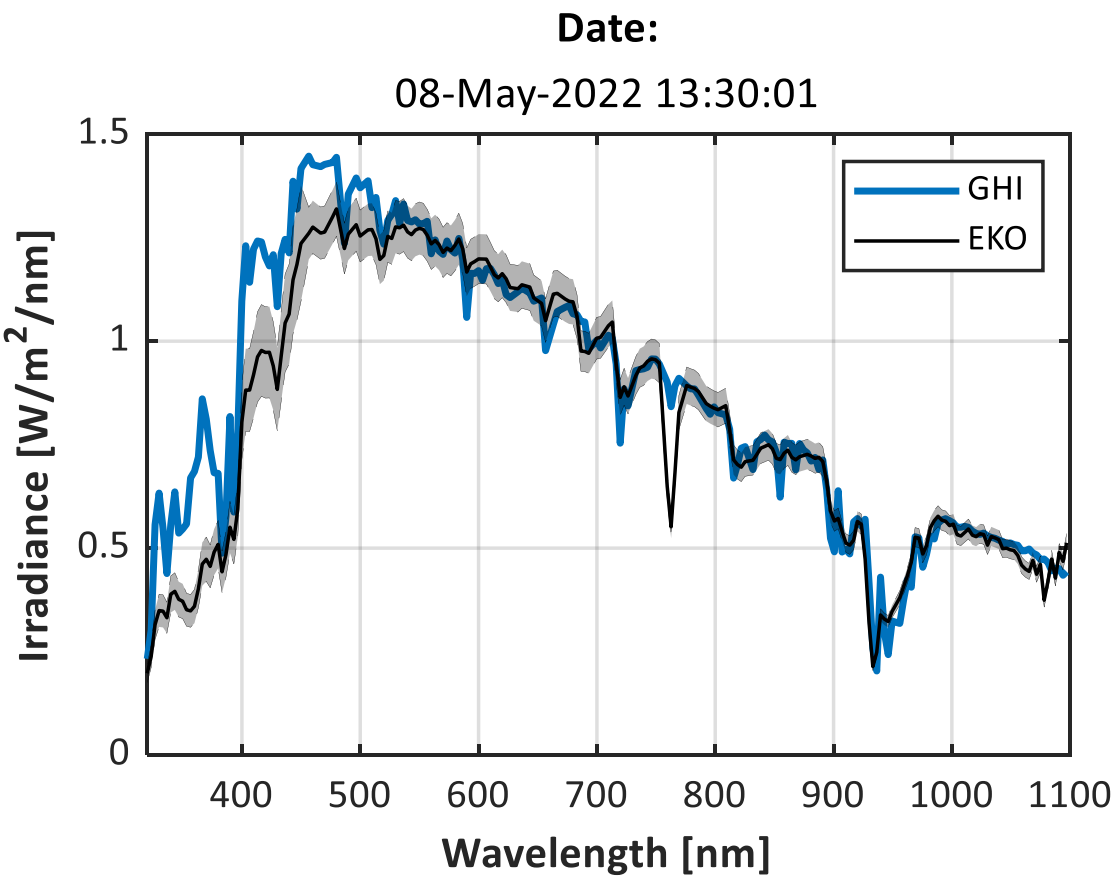


Figure 6.1: Reconstruction result for the highest recorded irradiance point, where the blue thicker line GHI is the reconstructed irradiance, the thinner black line the EKO™ spectroradiometer measured irradiance and the grey shaded area the uncertainty range of the EKO™.

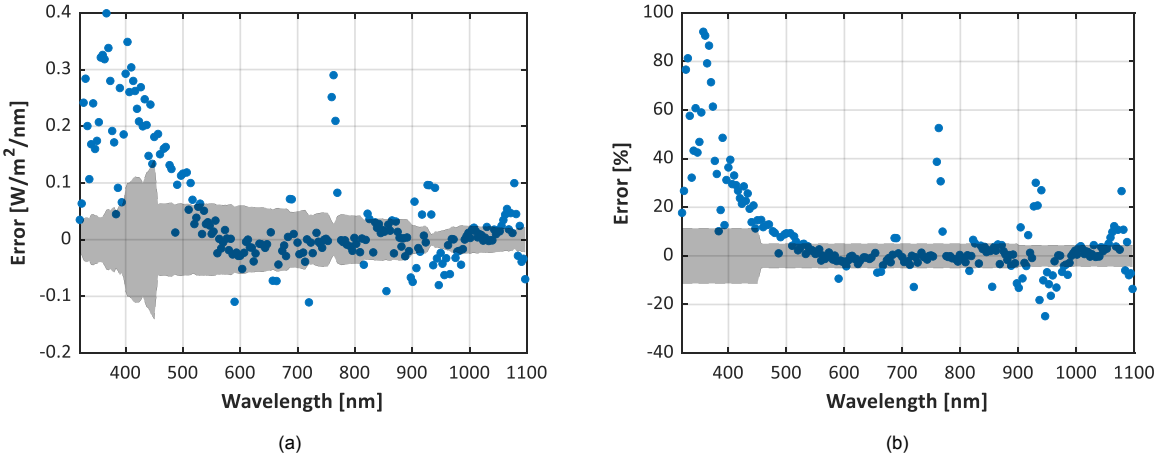


Figure 6.2: Reconstruction errors for the highest recorded irradiance point, where the blue points are the spectral reconstruction error and the grey shaded area the uncertainty range of the EKO™ measured data, with the absolute error in (a) and the relative error in (b)

To analyse the reconstruction model, data-points where the irradiance of the albedometer in the range of 320-1100 nm is lower than 400 W/m^2 were removed. This reduces the calibration error range from [≈-20, 30] W/m^2(Figure 5.12b) to [-15, 11.5] W/m^2 or [-5, 3.5] %, which reduces the impact of calibration errors on the reconstruction. Around 30% of the data-set is removed by doing this, there are 750 reconstructed spectra left. Figure 6.3a shows the 95% confidence interval of the absolute reconstruction errors and Figure 6.3b the relative error. Table 6.1 shows the average values of the 95% confidence interval ranges for the three sensor ranges and the total range. This table shows again that the error in the first wavelength range is the biggest. The relative error range of the third wavelength range is twice the range of the middle wavelength range, but the absolute average errors are similar. To compare the average errors with the reported EKO™ uncertainty, the average error is also determined for the wavelength ranges of 350-450,450-900 and 900-1050 nm in Table 6.2 which shows that the reconstruction errors are far greater than the EKO™ uncertainty.

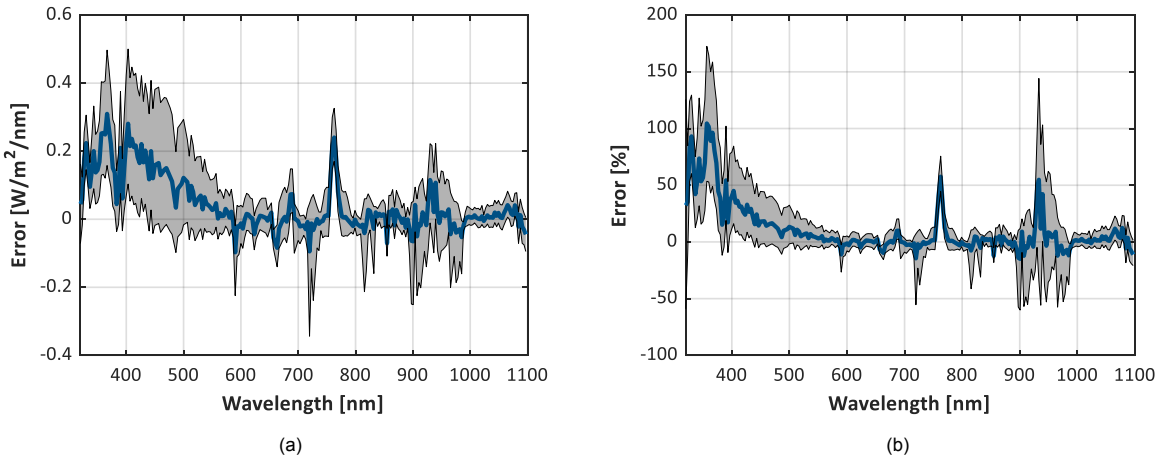


Figure 6.3: Mean error plotted in blue and 95% confidence interval of reconstruction error in $W/m^2/nm$ and % in (a) and (b) respectively

Table 6.1: Average 95% confidence interval reconstruction and the mean error in the three wavelength ranges and the total range

		Wavelength range [nm]			
		320-590	**590-850**	**850-1100**	**Total (320-1100)**
Absolute error [W/m^2/nm]	**Range**	[0.034, 0.304]	[-0.056, 0.066]	[-0.064, 0.063]	[-0.028, 0.147]
	Mean	0.156	0.009	0.004	0.058
Relative error [%]	**Range**	[10.2, 65.0]	[-7.7, 10.1]	[-17.2, 20.1]	[-4.9, 32.5]
	Mean	34.3	1.9	2.14	13.1

Table 6.2: The average spectral 95% confidence interval and the mean error of the reconstruction compared to the reported uncertainty of the EKO™ spectroradiometer

	Wavelength range [nm]		
	350-450	**450-900**	**900-1050**
Reconstruction average 95% error	[19.95, 96.02]	[-6.33, 13.98]	[-22.37, 25.86]
Reconstruction mean error	43.12	2.75	3.12
EKO™ uncertainty	±11.35	±5.00	±4.39

Figure 6.4a shows a reconstructed spectrum with a high deviation throughout the entire wavelength range, but especially in the first range of 320-590 nm the reconstructed spectrum deviates significantly. In this region the aerosol and ozone effect are determined by the reconstruction model. Between 320 and 450 nm only the aerosol affects the spectrum, which is underestimated if the reconstruction lies above the EKO™, in the region 450-590 also the ozone transmittance affects the spectrum. The bigger the drop from 450 to 590 nm, the bigger the ozone effect. Similarly, in the region of 700-1100 nm there are aerosol and water vapor effects. The downward peaks are due to water vapor effects and the height of the overall decreasing line is caused by aerosols. This line is above the EKO™ line, which means that also in this region the aerosol effect is underestimated. The water vapor peaks on the other hand are much bigger than the EKO™ reference, thus water vapor effect is overestimated in this reconstruction. In fact, the ozone reduced path-length and the total precipitable water reached their upper limits of 1 atm-cm and 12 cm respectively. Figure 6.4b shows the opposite scenario for the ozone and water vapour effects. In the range of 450-1100 nm there are almost no deviations from the standard decreasing trend. In this case the ozone reduced path-length and total precipitable water almost reached their lower limits of 0. The values are 0.001 atm-cm and 0.021 cm respectively. The decreasing trend is lower than the EKO™ measured spectrum, which indicates that the aerosol effect in this region is overestimated. However, in the region of 320-450 nm the reconstructed spectrum is higher than the measured spectrum, which indicates an underestimation of the aerosol effect. It appears that the aerosol transmittance is not properly described by the model since the effect on the spectrum is over and underestimated in different wavelength regions. Another possible reason is that the assumed concentrations of the trace gases are too low resulting in a too high trace gases transmittance (Figure 3.3b). However, the value of these concentrations must be set to values between moderate and severe pollution to have a noticeable effect on the spectrum (Gueymard, 2008). It was assumed that the pollution in Delft does not reach significantly high concentrations as the average air quality is quite good (PlumeLabs, n.d.). Finally, the errors could also be caused by the fact that the model uses an average albedo per wavelength range, rather than a spectral albedo. The albedo affects the back-scattered component from the diffuse irradiance. However the effect on the diffuse part is relatively small and the diffuse fraction of the GHI according to the reconstruction model are 2% for Figure 6.4a and 20% for Figure 6.4b, which makes it unlikely that the error is caused by the albedo.

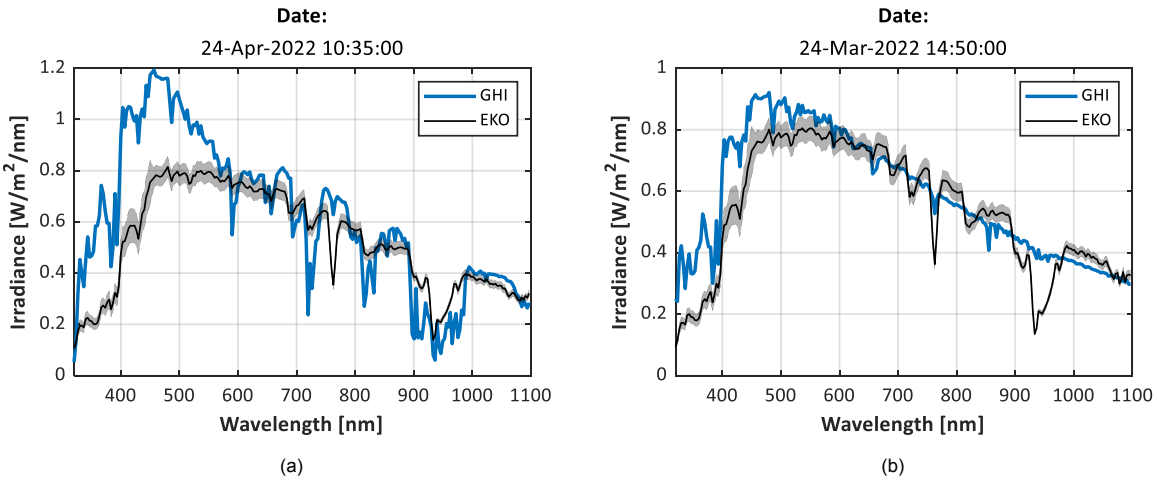


Figure 6.4: Two different reconstructed spectra compared to the EKO™ measurement and uncertainty range. The reconstructed spectrum in (a) reached the upper limits of the ozone reduced path-length and the total precipitable water, while the reconstructed spectrum in (b) approaches the lower limits.

The interdependence of the reconstruction in the three wavelength bands is clearly visible in Figure 6.5a and Figure 6.5b. There is only 5 minutes in between the two spectra and the EKO™ measured spectrum only changes slightly between the 2 measurements. The error in the 320-590 nm range in the left spectrum is bigger than the one in the right. Consequently the rest of the spectrum is also reconstructed with a bigger error, as the water vapor peaks centered just above 700 nm and between 900 and 1000 nm are better simulated in the right figure. This is also an indication that the model has difficulties with obtaining the best values for the optimization parameters if a part of the spectrum is not well defined by the model.

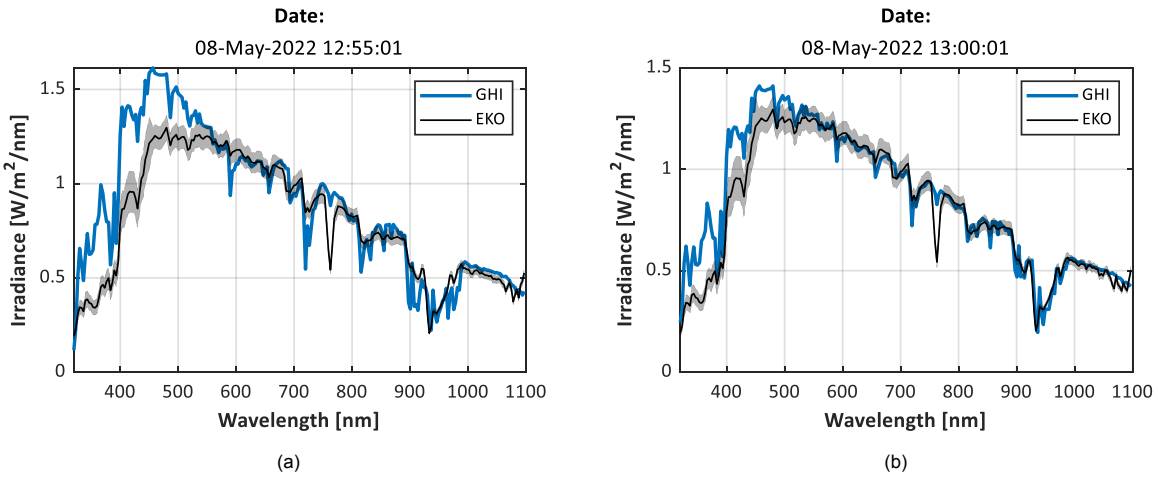


Figure 6.5: Two reconstructed spectra 5 minutes apart with similar measured spectra but with different reconstruction results.

From the 750 reconstructed spectra, there was one reconstruction that worked very well, with a mean absolute spectral reconstruction error of 8.34 %. The average of the entire data-set was 18.9 % and 95% was within 11.3 to 31.0 %. This spectrum is shown in Figure 6.6. The reconstructed spectrum manages to match the measured spectrum very well. Only the third region now contains some errors, in the water vapor peaks and the at 1000-1100 nm the aerosol effect is a little underestimated causing the slight upward shift from the measured spectrum. Although this spectrum is an outlier of the reconstructed spectra, it does raise the question what conditions caused this spectrum to be reconstructed this well, especially in the first region. It could be that only for this data point, the assumptions of the trace gases were accurate and for all other data-points should be increased significantly. As discussed before, this significant increase of trace gases was assumed to not be

true for Delft, where the air quality is quite good so there should be more moments where the air pollution is not high. If the trace gases were the cause of the errors, the reconstruction should have performed better far more data-points. Another possible reason is that the model is not constrained enough to cope with differences between the real spectra and uncertainties of the measurements and decomposed irradiance values compared to the SMARTS generated spectra. However, due to the fact that this accurately reconstructed spectrum was an outlier, the cause of the error is expected to be in the aerosol transmittance. The effect of the average albedo is small as discussed before, however the reconstruction model was tested with an adjustment to this albedo. The average albedo in the region of 320-590 nm was split into three average albedos in this range, these three average albedos were added as optimization parameters with ±30% as limits. These tests had practically no impact on the reconstruction performance.

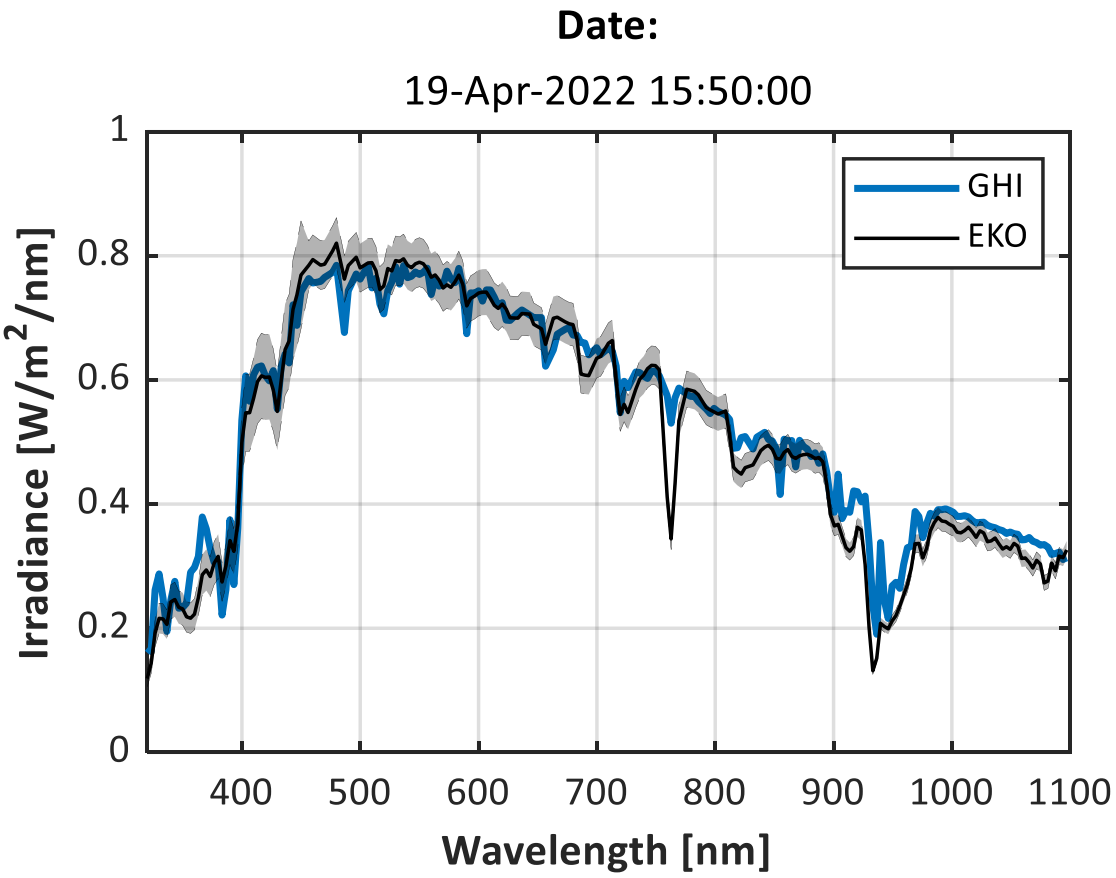


Figure 6.6: Reconstructed spectrum with the smallest average absolute spectral error (8.34%)

6.2. Modified reconstruction results

In an attempt to improve the reconstruction model, modification coefficients were added to the aerosol optical depth in the range of the first sensor. The number of modification parameters, the wavelength region they affected and the upper and lower bounds for the PSO were tested by trial-and-error and visually judging the new reconstructed spectra. This resulted in four modification factors m_i added to Equation 3.10 and shown in Equation 6.1. M_1 modifies $\tau_{a\lambda}$ from 320 to 403 nm with a constant value of 2.5. M_2 and M_3 modify the spectrum in the ranges of 429-499 and 499-590 nm respectively, with a value between 0.75 and 1.5, which is decided in the PSO. Finally, M_4 modifies $\tau_{a\lambda}$ from 429 to 499 nm, with a value between 0.75 and 2.5. Besides these modification factors, the weighting coefficients in Equation 4.1 were adjusted again to a_1 = 100, a_{11} = 100 a_{12} = 1,000, a_{13} = 1,000,a_2 = 20 and a_3 = 10.

$$\tau_{a\lambda} = M_i * \frac{\beta_i}{\lambda_i^{\alpha}} \tag{6.1}$$

The modified model was tested with the same 1062 data-points, after which the points where the 320-1100 nm irradiance was lower than 400 W/m^2 were removed again. Although the new reconstruction model gave the PSO 3 additional unknown parameters to determine, the reconstruction of all the datapoints only took 13 hours and 40 minutes, an average of 46 seconds per reconstruction compared to 1 minute in the standard reconstruction model. In Figure 6.7, Figure 6.8a and Figure 6.8b the reconstructed spectrum and the errors of the same point as in Figure 6.1 is shown. The reconstruction is now closer to the EKO™ measured spectrum than the results from Figure 6.1.

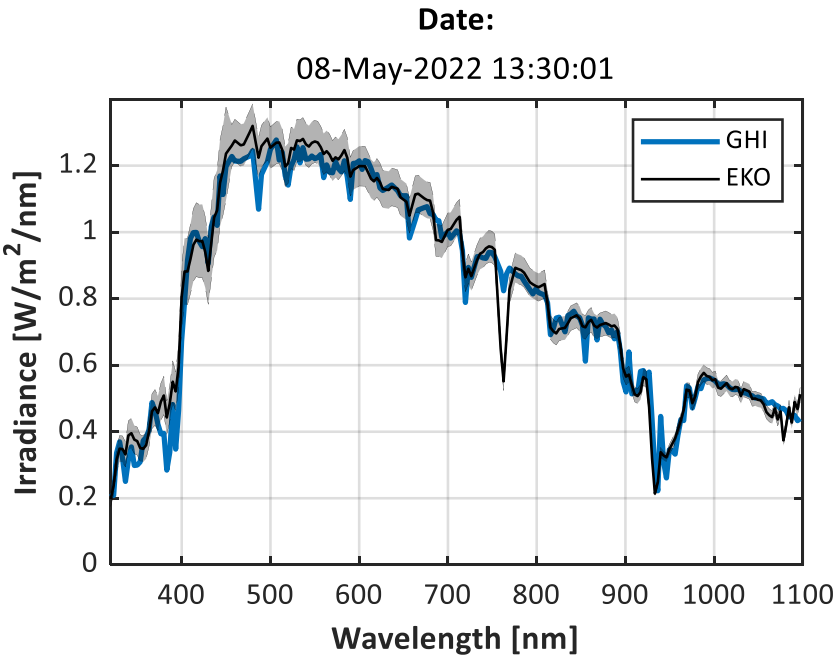


Figure 6.7: Reconstruction errors for the highest recorded irradiance point, where the blue points are the spectral reconstruction error and the grey shaded area the uncertainty range of the EKO™ measured data, with the absolute error in (a) and the relative error in (b)

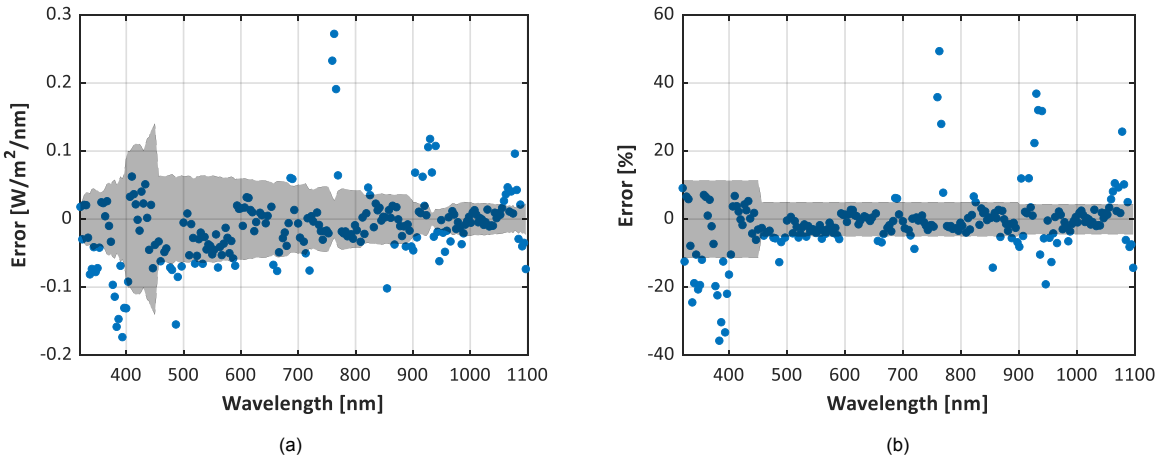


Figure 6.8: Reconstruction errors for the highest recorded irradiance point, where the blue points are the spectral reconstruction error and the grey shaded area the uncertainty range of the EKO™ measured data, with the absolute error in (a) and the relative error in (b)

In Figure 6.9a and Figure 6.9b the reconstructed spectra of the modified model for the data-points where the initial reconstruction model resulted in high errors (Figure 6.4a and Figure 6.4b) are shown. In the left spectrum the reconstruction has significantly improved compared to Figure 6.4a, not only in the 320 to 590 nm part, but also the water vapor effect is now simulated accurately. The spectrum in the right figure still neglects the water vapor effect despite the fact that the reconstruction between 320 and 590 nm has improved compared to Figure 6.4b. In Figure 6.10a and Figure 6.10b the two spectra, 5 minutes apart, where the original reconstruction model showed inconsistent results. The reconstructed spectra from the modified model now show to identical spectra.

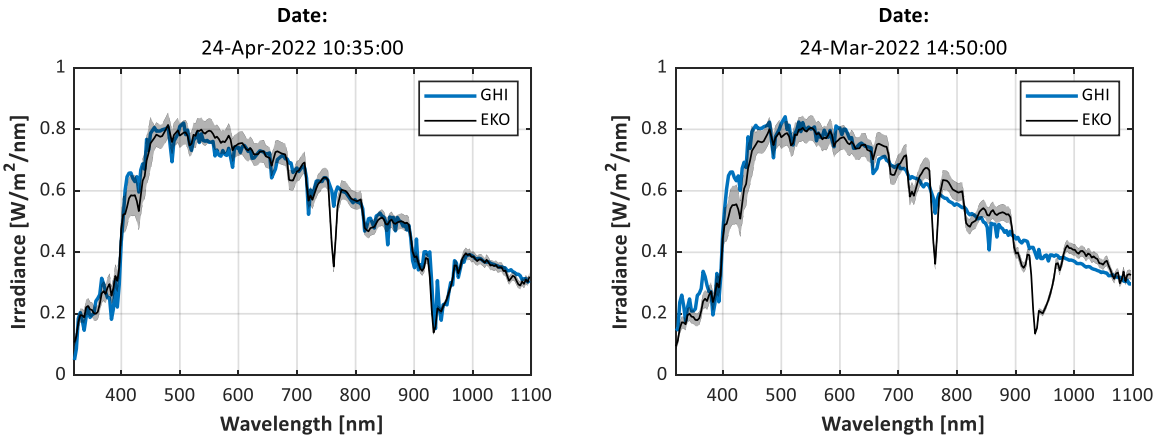


Figure 6.9: The improved reconstruction of Figure 6.4a in (a) and in (b) the new reconstruction from Figure 6.4b where the error in the 320-590 nm range is reduced but where the errors in the 650-1100 nm range are not improved.

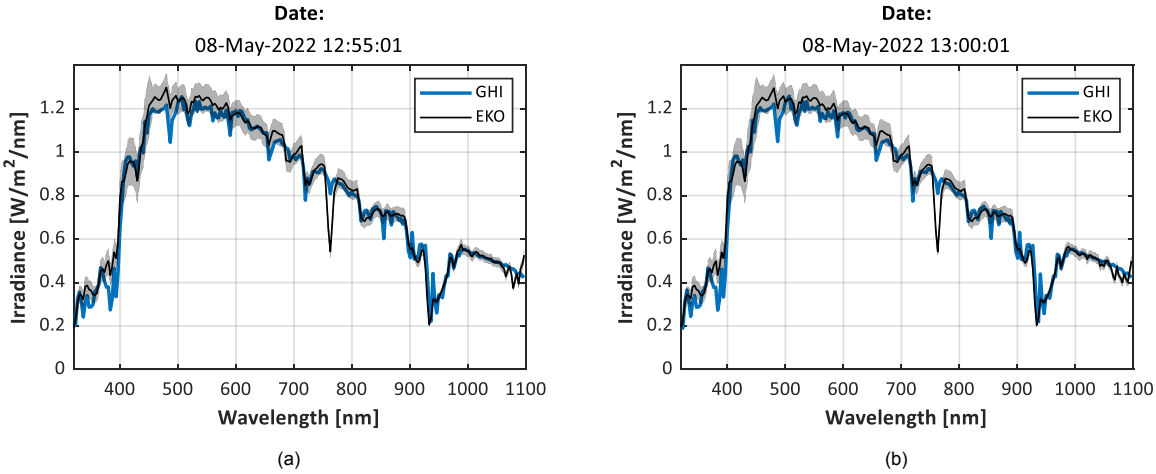


Figure 6.10: Two reconstructed spectra 5 minutes apart with similar measured spectra but with different reconstruction results.

In Figure 6.11 the spectrum of the modified model is shown, for the data-point where the original model achieved a very good reconstruction. In this case, the modified model does not perform as well as the original model. The modification factors applied to the first region (320-590 nm) cause the spectrum to be poorly reconstructed in this section, and consequently also reduces the accuracy of the reconstruction in the rest of the spectrum.

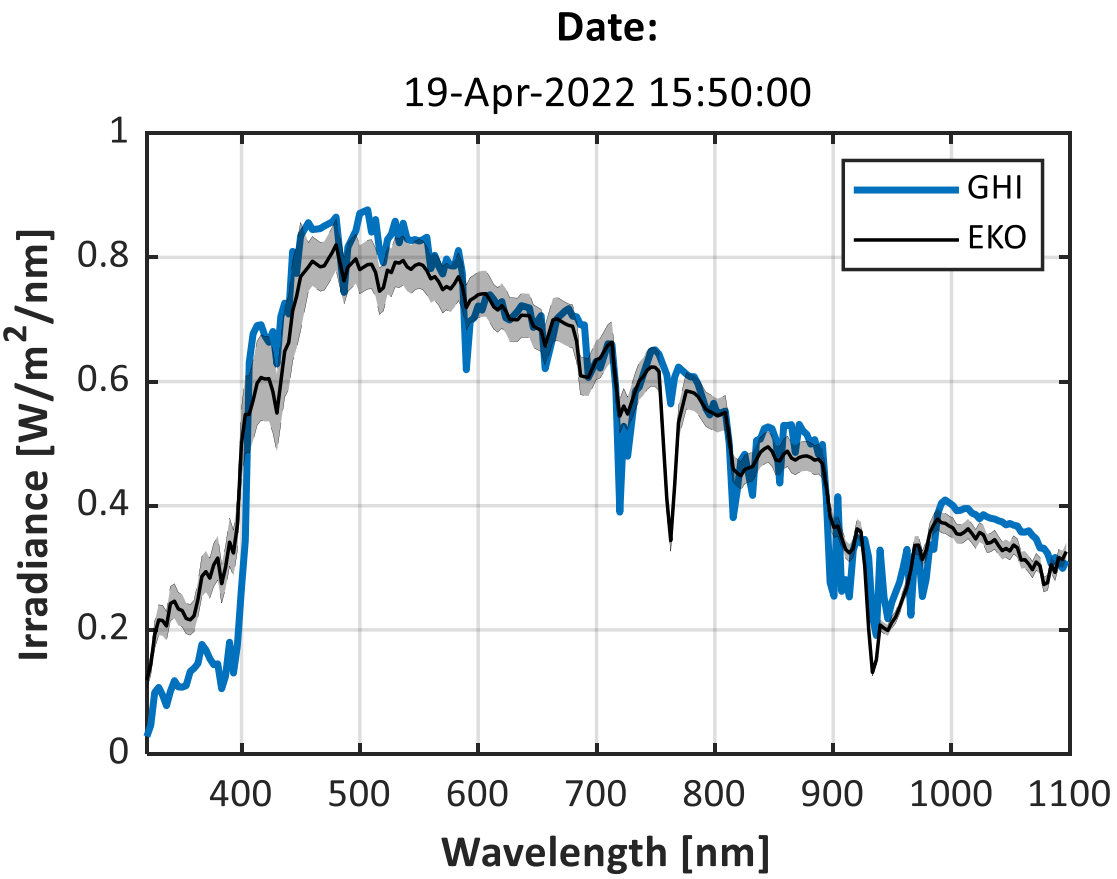
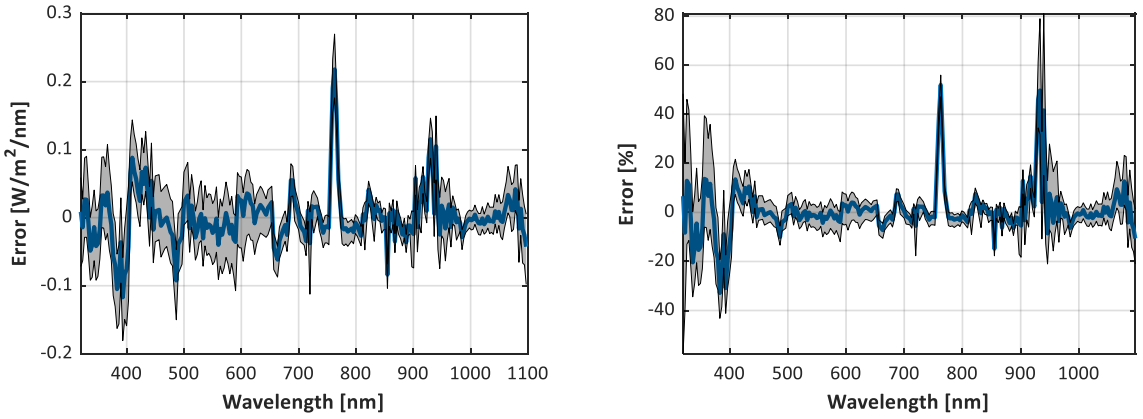


Figure 6.11: Reconstructed spectrum with the smallest average absolute spectral error (8.34%)

Figure 6.12a and Figure 6.12b show the mean and 95% confidence interval of the reconstruction error for the entire dataset, again with irradiances below 400 W/m^2 in the 320-1100 nm range removed. The errors are now a lot smaller and not only in the 320-590 nm range where the modification factors were applied, but also in the rest of the spectrum. Table 6.3 and Table 6.4 show the average reconstruction errors for the different wavelength ranges again. The overall performance of this modified reconstruction model has improved significantly compared to the original model and the accuracy is now approaching the reported uncertainty of the EKO™ spectroradiometer. It could however be the case that while applying the modification factors, the model is over-fitted to the current data-set of 750 spectra. The results do however prove that if the reconstruction in the first region (320-590 nm) is improved, the reconstruction in of the rest of the spectrum is also improved.



(a) (b)

Figure 6.12: Mean error plotted in blue and 95% confidence interval of reconstruction error in $W/m^2/nm$ and % in (a) and (b) respectively

Table 6.3: Average 95% confidence interval reconstruction and the mean error in the three wavelength ranges and the total range

		Wavelength range [nm]			
		320-590	**590-850**	**850-1100**	**Total (320-1100)**
Absolute error [W/m²/nm]	**Range**	[-0.055, 0.043]	[-0.021, 0.032]	[-0.022, 0.029]	[-0.033, 0.035]
	Mean	-0.008	0.010	0.004	0.002
Relative error [%]	**Range**	[-11.3, 9.1]	[-2.1, 4.9]	[-4.6, 10.1]	[-6.2, 8.2]
	Mean	-1.9	2.1	2.3	0.82

Table 6.4: The average spectral 95% confidence interval and the mean error of the modified reconstruction compared to the reported uncertainty of the EKO™ spectroradiometer

	Wavelength range [nm]		
	350-450	**450-900**	**900-1050**
Reconstruction average 95% error	[-11.62, 11.87]	[-3.92, 3.73]	[-3.3, 12.75]
Reconstruction mean error	-1.43	0.43	4.07
EKO™ uncertainty	±11.35	±5.00	±4.39

7

Conclusions and recommendations

7.1. Conclusions

The goal of this thesis was to design a spectral reconstruction model in MATLAB that uses limited spectral measurement data from an albedometer designed in two previous Master theses to reconstruct the clear-sky solar spectrum received at the top of the albedometer. The research questions were:

- What is the reconstruction accuracy of clear-sky solar spectra incident on the top of the PVMD albedometr, compared to the performance of the EKO spectroradiometer?
- What parameters are required for the model to reconstruct spectra?
- Are the current three sensors well-placed or should additional sensors be added?

The design of the reconstruction model was based on the Simple Model for Atmospheric Radiative Transfer of Sunshine (SMARTS) that can simulate solar spectrum if provided with accurate inputs for atmospheric constituents and the approach of Spectrafy™, a company that has successfully implemented simulation software with irradiance sensors that measure specific points in the spectrum to isolate atmospheric effects to reconstruct solar spectra under all sky conditions.

The reconstruction model designed in this Thesis uses a Particle Swarm Optimisation (PSO) algorithm, an algorithm that tries to find a global minimum of a function with particles spread across an n-dimensional space for n unknown parameters. These particles are inspired on a group of animals that communicate with each other to find a location with the most food. Three unknown parameters were defined in this thesis, the aerosol optical depth at 550 nm, the ozone reduced pathlength and the total precipitable water. These parameters are needed to determine the Aerosol, Ozone and Water vapor spectral transmittances. Spectral transmittances determine the fraction of the light that is transmitted through the atmosphere. For the error function, reference irradiance values are needed. These are created with the albedometer measurements, calibrated with an EKO™ spectroradiometer. Global horizontal irradiances and average albedo valuesin the ranges 320-1100, 320-590, 590-850 and 850-1100 nm were obtained. With a decomposition model (BRL), the global horizontal irradiance is decomposed into its two components, the direct normal irradiance and the diffuse horizontal irradiance for the range of 320-1100 nm to create more reference values. During each iteration of the PSO algorithm each particle creates a spectrum, which is evaluated by the error function. After each run the path of the particles is changed and the new spectrum is evaluated again. After a certain amount of iterations the error function converges to its minimum and the optimum values for the optimization parameters are determined, which are then used to create the spectrum. The reconstruction model was tested for 750 clear-sky spectra, after removing 30% of the original 1062 spectra where the irradiance in the range of 320-1100 nm was lower than 400 W/m^2. The reconstruction model failed in the 320-590 nm range, after which 4 modification coefficients were added to the model, resulting in a significant improvement in the accuracy of the reconstructed spectra.

The answers to the three research questions are:

- For clear-sky irradiances above 400 W/m^2, the original reconstruction model did not perform close to the EKO™ performance. The adjusted model did however perform within the uncertainty bounds of the spectroradiometer in the 450-900 nm range, in the 350-450 nm range it performed less then 0.5% outside the uncertainty bounds and for the 900-1050 nm range the upper bound is violated with ≈8 %.
- Next to the latitude,longitude and pressure, the reconstruction model requires the temperature and relative humidity to be able to reconstruct a spectrum.
- The original reconstruction model failed in the reconstruction of the 320-590 nm range. Although the modified model improved the reconstruction, the modifications could be overfitted to the current dataset. Placing additional sensors in the 320-590 region could help in identifying the cause of the error in this region and put more constraints on the optimization algorithm.

7.2. Recommendations

The calibration of the albedometer contained some high errors with respect to the EKO™ spectroradiometer. For the clear-sky data-set with low irradiances removed the error was relatively small, but points with higher errors can affect the reconstruction. A new calibration with the re-calibrated spectroradiometer could improve this and perhaps positioning the albedometer and spectroradiometer to a fixed surface, and not a sun-tracker could also improve the calibration.

The modified reconstruction model contains promising reconstruction errors with respect to the measured EKO™ spectroradiometer spectra. However the modification was done by trial-and-error and could be specific to this single data-set. It is therefore recommended to investigate the cause of the reconstruction error in the wavelength range of 320-590 nm first. The first step is to test the reconstruction model with the new re-calibrated spectroradiometer to find if this was the cause for the reconstruction error.

If the spectroradiometer not working properly is not the cause of the errors, it is most likely caused by either the aerosol transmittance or by the trace gas transmittance. The trace gases (HNO_3, NO_2, NO_3, SO_2, BrO, CH_2O, HNO_2 and $ClNO_3$ only have an effect when their concentrations are classified between moderate and severe air pollution. This was assumed to not be the case for Delft but could be further investigated. If the aerosol transmittance causes the the error, it would mean that the calculations from the model, or SMARTS are not valid for the conditions during the dataset in that wavelength range. A possible solution could be to simplify the aerosol transmittance calculations in the region 320-590 nm. Especially below 499 nm, where the coefficients for the aerosol transmittance change.

The third recommendation is about the placement of additional sensors. If the error in the lower wavelength region is not caused by possible malfunction of the spectroradiometer, it is advised to place (an) additional sensor(s) in this region. a photodiode with a long-pass filter with a cut-off frequency of 500 nm will lead to two additional irradiance reference values, 320-499 nm and 500-599 nm. This could also prove the inaccurate description of the aerosol transmittance in the 320-499 nm range. A different approach however is to make a spectral albedometer from the two EKO™ spectroradiometers. This way virtual sensors can be created that measure different parts of the spectrum and once the reconstruction works properly the new albedometer with the additional sensor(s) will only have to designed once. Furthermore, calibration errors are removed and the calibration of the bottom sensors of the albedometer can be done with the EKO™ spectroradiometer facing down, which is now calibrated with the same calibration as the upward facing spectroradiometer. The EKO™ spectral albedometer can also be used in future research for the reconstruction of the spectrum received by the downward facing albedometer sensor.

The current model has implemented SMARTS, a clear-sky spectral simulation model. The Spectrafy™ approach, which uses the same optimization parameters, but with a different approach. To test the model designed in this thesis under different sky-conditions, it is recommended to utilize the sky-classification model that Gijs van Urk is developing for his master thesis. He is developing a sky-classification model with 5 classes, rather than the three that are usually used (clear, partly cloudy and fully overcast). This will give a better overview of situations where the model might be failing.

Bibliography

Adyatama, A. (2019). *Particle swarm optimization*. https://rpubs.com/argaadya/intro-pso (accessed: 26.09.2022)

Bird, R. (1984). A simple, solar spectral model for direct-normal and diffuse horizontal irradiance. *Solar Energy*, *32*(4), 461–471. https://doi.org/10.1016/0038-092X(84)90260-3

Boland, J., Huang, J., & Ridley, B. (2013). Decomposing global solar radiation into its direct and diffuse components. *Renewable and Sustainable Energy Reviews*, *28*, 749–756. https://doi.org/10.1016/j.rser.2013.08.023

Brennan, M., Abramese, A., Andrews, R., & Pearce, J. (2014). Effects of spectral albedo on solar photovoltaic devices. *Solar Energy Materials and Solar Cells*, *124*, 111–116. https://doi.org/10.1016/j.solmat.2014.01.046

EKO. (n.d.). *Ms-711 spectroradiometer*. https://www.eko-instruments.com/eu/categories/products/spectroradiometers/ms-711-spectroradiometer (accessed: 18.09.2022)

Fieducik, J. (2019). The use of solar radiation for generating heat in a solar air collector in northern poland. *E3S Web Conf.*, *100*. https://doi.org/10.1051/e3sconf/201910000016

Gueymard, C. A. (1993). Development and performance assessment of a clear sky spectral radiation model. *Solar Conference, American Solar Energy Society*. https://www.researchgate.net/publication/236314809_Development_and_performance_assessment_of_a_clear_sky_spectral_radiation_model

Gueymard, C. A. (Ed.). (1995). *Smarts2, a simple model of the atmospheric radiative transfer of sunshine: Algorithms and performance assessment*. Florida Solar Energy Center. https://www.researchgate.net/publication/236314775_SMARTS2_a_simple_model_of_the_atmospheric_radiative_transfer_of_sunshine_algorithms_and_performance_assessment

Gueymard, C. A. (2001). Parameterized transmittance model for direct beam and circumsolar spectral irradiance. *Solar Energy*, *71*(5), 325–346. https://doi.org/10.1016/S0038-092X(01)00054-8

Gueymard, C. A. (2006). Prediction and validation of cloudless shortwave irradiance spectra for horizontal, tilted, or tracking receivers. *Solar Conference, American Solar Energy Society*. https://www.arm.gov/publications/tech_reports/handbooks/rss/publications/ASES2006_Gueymard.pdf

Gueymard, C. A. (2008). Smarts version 2.9.5.i13. https://www.nrel.gov/grid/solar-resource/smarts.html

Gueymard, C. A., & Myers, D. R. (2004). Description and availability of the smarts spectral model for photovoltaic applications. *International Symposium on Optical Science and Technology*. https://www.nrel.gov/docs/gen/fy04/36320.pdf

Hukseflux. (n.d.). *Pyranometers, solar radiation sensors*. https://www.hukseflux.com/products/pyranometers-solar-radiation-sensors (accessed: 18.09.2022)

Hukseflux. (2006). What is a pyranometer? *Solar Energy*. https://www.hukseflux.com/uploads/inline/note-what_is_a_pyranometer_v2006.pdf

IEA. (2022). *Renewable energy market update - outlook for 2022 and 2023* (May).

Institute, U. S. (n.d.). *Pyranometer*. https://www.myussi.com/glossary/pyranometer/ (accessed: 25.09.2022)

Kaul, A. (2020). *Design and fabrication of an irradiance sensor for bifacial pv* (Msc. Thesis). Delft University of Technology.

Kipp & Zonen. (n.d.). *Solar instruments*. https://www.kippzonen.com/ProductGroup/1/Solar-Instruments (accessed: 18.09.2022)

MathWorks. (2022). *Boxplot*. https://nl.mathworks.com/help/stats/boxplot.html#mw_712e4076-f8d1-4e11-bcf7-5f79da6fe537 (accessed: 28.09.2022)

NASA. (n.d.). *Ecostress spectral library*. https://speclib.jpl.nasa.gov/library (accessed: 1.10.2022)

NOAA. (2021). *Despite pandemic shutdowns, carbon dioxide and methane surged in 2020*. https://research.noaa.gov/article/ArtMID/587/ArticleID/2742/Despite-pandemic-shutdowns-carbon-dioxide-and-methane-surged-in-2020#:~:text=The%5C%20global%5C%20surface%5C%

20average%5C%20for,%5C%2C%5C%201998%5C%2C%5C%202015%5C%20and%5C%202016. (accessed: 24.09.2022)

Optics, A. (n.d.). *Why is the sky blue?* https://atoptics.co.uk/atoptics/blsky.htm (accessed: 28.09.2022)

PlumeLabs. (n.d.). *Air quality in delft*. https://air.plumelabs.com/air-quality-in-Delft-bzjj (accessed: 01.10.2022)

PVPerformance. (n.d.). *Pv_lib toolbox*. https://pvpmc.sandia.gov/applications/pv_lib-toolbox/ (accessed: 23.09.2022)

REINDL, D. T., BECKMAN, W. A., & DUFFLE, J. A. (1990). Diffuse fraction correlations. *Solar Energy*, *45*(1), 1–7. https://www.lmd.polytechnique.fr/~drobinski/MEC573/2021/Project_Solar_France/biblio/Reindl%5C%20et%5C%20al.%5C%20-%5C%201990%5C%20-%5C%20Diffuse%5C%20fraction%5C%20correlations.pdf

Ridley, B., Boland, J., & Lauret, P. (2010). Modelling of diffuse solar fraction with multiple predictors. *Renewable Energy*, *35*(2), 478–483. https://doi.org/10.1016/j.renene.2009.07.018

Rohde, R. A. (2013). *Spectrum of solar radiation (earth)*. https://commons.wikimedia.org/w/index.php?curid=24648395 (accessed: 19.09.2022)

Romero Olvera, A. (2021). *Bio-inspired design and fabrication of a spectrally resolved albedometer* (Msc. Thesis). Delft University of Technology.

Sandhu, J. (2022). *Bifacial solar panels: Innovative and more efficient*. https://www.solarreviews.com/blog/bifacial-solar-panels (accessed: 02.10.2022)

Smets, A., Jäger, K., Isabella, O., van Swaaij, R., & Zeman, M. (Eds.). (2016). *Solar energy the physics and engineering of photovoltaic conversion technologies and systems*. UIT Cambridge Ltd.

Society, A. M. (n.d.). *Rayleigh scattering*. https://glossary.ametsoc.org/wiki/Rayleigh_scattering (accessed: 18.09.2022)

Solar Anywhere. (2021). *Definitions*. https://www.solaranywhere.com/support/data-fields/definitions/ (accessed: 19.09.2022)

Spectrafy. (n.d.). *Products*. https://www.spectrafy.com/products (accessed: 18.09.2022)

Tam, A. (2021). *A gentle introduction to particle swarm optimization*. https://machinelearningmastery.com/a-gentle-introduction-to-particle-swarm-optimization/ (accessed: 26.09.2022)

Tatsiankou, V., Hinzera, K., Mohammeda, J., Murona, A., Wilkinsa, M., Haysoma, H., J. amd Schriemera, & Myrskogb, S. (2014). Reconstruction of solar spectral resource using limited spectral sampling for concentrating photovoltaic systems. *Proc SPIE*, *8915*, 06–. https://doi.org/10.1117/12.2033613

VDMA. (2022). *International technology roadmap for photovoltaic (ITRPV) 2021 results* (13th).

Xie, Y., & Sengupta, M. (2019). A fast all-sky radiation model for solar applications with narrowband irradiances on tilted surfaces (farms-nit): Part i. the clear-sky model. *Solar Energy*, *188*, 799–812. https://doi.org/10.1016/j.solener.2019.06.058

Xie, Y., Sengupta, M., & Wang, C. (2019). A fast all-sky radiation model for solar applications with narrowband irradiances on tilted surfaces (farms-nit): Part ii. the cloudy-sky model. *Solar Energy*, *188*, 799–812. https://doi.org/10.1016/j.solener.2019.06.058

Ziar, H., Fatih Sönmez, F., Isabela, O., & Zeman, M. (2019). A comprehensive albedo model for solar energy applications: Geometric spectral albedo. *Applied Energy*, *255*. https://doi.org/10.1016/j.apenergy.2019.113867